Mapping Arctic Sea Ice Thickness: A New Method for Improved Ice Freeboard Retrieval from Satellite Altimetry

Jack C. Landy[1,2*]; Jerome Bouffard[3], Chris Wilson[4], Stefanie Rynders[5]; Yevgeny Aksenov[5]; Michel Tsamados[6]

[1] Bristol Glaciology Centre, School of Geographical Sciences, University of Bristol, Bristol BS8 1SS, U.K.

[2] Now at: Centre for Integrated Remote Sensing and Forecasting for Arctic Operations (CIRFA), Department of Physics and Technology, University of Tromsø: The Arctic University of Norway

[3] European Space Agency, European Space Research Institute (ESRIN), Frascati, Italy

[4] National Oceanography Centre, Liverpool, UK

[5] National Oceanography Centre, Southampton, UK

[6] Centre for Polar Observation and Modelling, Department of Earth Sciences, University College London, UK

* Corresponding Author: Jack Landy, Email: jack.landy@bristol.ac.uk

Key Points:

- Lead observations from neighboring altimeter tracks are exploited to improve the sea surface height calculated at ice-covered locations
- The interpolation is constrained with sea surface decorrelation length- and time-scales from CryoSat-2 data and ice-ocean model simulations
- Altimeter sampling of multi-track leads improves the precision of Arctic sea ice freeboards by 20% and can increase accuracy by up to 25%

Abstract

A growing number of studies are concluding that the resilience of the Arctic sea ice cover in a warming climate is essentially controlled by its thickness. Satellite radar and laser altimeters have allowed us to routinely monitor sea ice thickness across most of the Arctic Ocean for several decades. However, a key uncertainty remaining in the sea ice thickness retrieval is the error on the sea surface height (SSH) which is conventionally interpolated at ice floes from a limited number of lead observations along the altimeter's orbital track. Here, we use an objective mapping approach to determine sea surface height from all proximal lead samples located on the orbital track and from adjacent tracks within a neighborhood of 10s of kilometers. The patterns of the SSH signal's zonal, meridional, and temporal decorrelation length scales are obtained by analyzing the covariance of historic CryoSat-2 Arctic lead observations, which match the scales obtained from an equivalent analysis of high-resolution sea ice-ocean model fields. We use these length scales to determine an optimal SSH and error estimate for each sea ice floe location. By exploiting leads from adjacent tracks, we can increase the SSH precision estimated at orbital crossovers by a factor of three. In regions of high SSH uncertainty, biases in CryoSat-2 sea ice freeboard can be reduced by 25% with respect to coincident airborne validation data. The new method is not restricted to a particular sensor or mode, so it can be generalized to all present and historic polar altimetry missions.

Plain Language Summary

Arctic Ocean sea ice thickness has been measured with satellite altimeters for several decades by stitching together observations of the sea level at open water leads or ‘cracks’ in the ice. The height difference between the sea ice surface and sea level, known as the freeboard, can then be converted to an estimate for the ice thickness. However, open water lead observations can be hundreds of kilometers apart along the satellite’s orbit, so here we develop a new method which also uses leads on nearby orbits to improve the sea level estimate at ice-covered locations. This requires us to understand how rapidly the Arctic sea level varies over space and time, which we do using ESA’s CryoSat-2 satellite radar altimeter. With an optimal processing method that exploits 10-100s of times more observations than normal, we can treble the precision of the sea level estimated ‘under’ sea ice. Up to 25% improvement in sea ice freeboard further indicates that the new method could upgrade current and historic altimetry-derived Arctic sea ice thickness records.

1. Introduction

Sea ice extent in the Northern Hemisphere has been declining at an increasingly alarming rate for more than two decades now (Parkinson & DiGirolamo, 2016). Recent studies have recognized that trends and interannual variations in ice extent are extremely sensitive to the pan-Arctic distribution of sea ice thickness (Rae, et al., 2014; Castro-Morales, et al., 2014). The transition from a sea ice cover dominated by thicker, multi-year ice in the 1980s to an ice cover dominated by thinner, first-year ice in the present day (Tschudi, et al., 2016) has amplified interannual fluctuations in the sea ice extent (Stroeve, et al., 2018). It has been demonstrated that seasonal forecasts for the sea ice area can be strikingly improved by initializing numerical models with ice thickness observations (Msadek, et al., 2014; Massonnet, et al., 2015; Allard, et al., 2018; Blockley & Peterson, 2018; Fritzner, et al., 2019; Schröder, et al., 2019).

Sea ice thickness has been estimated with satellite radar altimeters, including ERS-1/-2 and Envisat RA-2, and laser altimeters, including ICESat, for more than three decades (Quartly, et al., 2019). With the launch of the European Space Agency (ESA) CryoSat-2 mission in 2010 (Wingham, et al., 2006) and the National Aeronautics and Space Administration (NASA) ICESat-2 mission in 2018 (Markus, et al., 2017), we are now in a position to monitor Arctic sea ice thickness up to 88 degrees latitude, covering the full basin on a monthly basis. These missions can provide sea ice thickness information for climate monitoring and sea ice trend analysis (Kwok, 2018), assimilation into Numerical Weather Prediction (NWP) systems (Blockley & Peterson, 2018), evaluating risk for polar marine vessels (Rinne & Similä, 2016), and predicting light-availability under sea ice for Arctic primary production (Stroeve, et al., 2021). The value of these sea ice thickness observations to the scientific community and commercial sector, e.g. shipping companies navigating Arctic routes, offshore marine operators and insurers (Melia, et al., 2016; Aksenov, et al., 2017), along with the success of the CryoSat-2 mission (Parrinello, et al., 2018), have motivated the European Commission to support the development of the satellite CRISTAL: Copernicus Polar Ice and Snow Topography Altimeter. If approved, the CRISTAL mission will carry a dual-frequency altimeter to measure the sea ice thickness and overlying snow depth simultaneously (Kern, et al., 2020).

Sea ice thickness can be estimated from measurements of the ice freeboard – the height of a sea ice floe above sea level – taken by a satellite radar or laser altimeter, such as CryoSat-2 or ICESat-2. Sea ice freeboard is converted to thickness with estimates for the sea ice density, and the depth and density of

snow accumulating at the ice surface. Since the level sea ice floes are typically no more than five meters in thickness (Laxon, et al., 2013), small variations in the measured sea ice floe height, sea surface height, or estimated snow depth or density can readily introduce systematic uncertainty in the derived ice thickness order 10-30% (Landy, et al., 2020). Methodological differences in the processing chain or in the auxiliary observations used in various algorithms can therefore lead to systematic differences in derived sea ice thickness of more than a meter (Sallila, et al., 2019). This is large enough to obscure long-term climate trends in the Arctic sea ice thickness (Kwok & Cunningham, 2015).

One of the largest sources of uncertainty in sea ice thickness estimates from altimetry is introduced in the measurement of the sea surface height (SSH). The SSH is defined as the ocean free surface elevation with respect to a reference ellipsoid at a sea ice floe and is conventionally interpolated for all ice-covered locations from sea surface tie-points located at the closest leads, i.e. openings in the sea ice pack, along the altimeter's orbital track (Laxon, et al., 2003; Kwok, et al., 2007). Uncertainty in the SSH can be estimated from height variations derived from altimeter returns at leads within a moving window applied along the track (Ricker, et al., 2014) (further details in Section 2). However, distances between an ice-covered sample and its closest lead can exceed 200 km along track, particularly in the compact pack ice (concentration >98%) of the Central Arctic Ocean (Wernecke & Kaleschke, 2015). In these cases, the SSH uncertainty is constrained only by the deviation of the interpolated sea surface from the local mean measured elevation and can reach 50 cm, varying considerably across the Arctic (Ricker, et al., 2014). Importantly, these interpolation uncertainties are highly correlated over distances of hundreds of kilometers (Tilling, et al., 2018), owing to the sparse distribution of leads along track (Wernecke & Kaleschke, 2015) and long-wavelength errors in the orbital or geophysical (e.g. earth and ocean tides) corrections used to process the altimeter observations (Wingham, et al., 2006). So, these errors only reduce in quadrature with the averaging of multiple tracks, rather than the total number of samples (Tilling, et al., 2018; Lawrence, et al., 2018). Averaged to a 25-km grid, the SSH error ranges from approximately 1 to 12 cm.

For several applications, including the reconciliation of sea ice mass balance, polar sea level, climate, and oceanography for scientific purposes and for commercial activities such as operational navigation, accurate determination of the SSH and its uncertainty in ice-covered waters are crucial. In regions with low lead density and high SSH uncertainty, derived freeboards can include long-distance spatially correlated biases (Xia & Xie, 2018). Such biases may either amplify or cancel each other out in different locations, for instance when estimating snow depth from centimeter-scale differences between

radar and laser sea ice freeboards (Kwok, et al., 2020). Here, we present a new approach for the accurate determination of the SSH which exploits all available lead observations from both the orbital track in focus and additional neighboring tracks. Although we use CryoSat-2 observations to demonstrate the method, the approach can be applied to any contemporary or historical satellite laser or radar altimetry mission (both pulse-limited and SAR). In Section 2 we give an overview of the conventional approaches for estimating the SSH and its uncertainty in sea ice-covered regions. Here we also discuss sources of random and systematic error in SSH observations. In Section 3 we introduce the satellite and airborne data sets used within our study. In Section 4 we analyze multi-year mean patterns of the Arctic Ocean SSH's spatial and temporal decorrelation length scales from CryoSat-2 lead observations. We then compare these length scales to patterns derived from a high-resolution, nominally 1/12 deg. (~ 4km in the Arctic), simulation of a coupled sea ice-ocean model within the NEMO (Nucleus for European Modelling of the Ocean) framework, where the sea ice component is LIM2 (Louvain-le-Neuve sea ice model version 2) and the ocean component is OPA (Ocean Parallélisé). We combine these length scales with the error estimates for SSH observations in Section 5 to determine the optimal instantaneous SSH at sea ice samples, through objective analysis of all proximal lead observations on both the track in focus and neighboring tracks. Section 6 compares the new SSH mapping scheme with a conventional scheme for March 2013. Section 7 validates our results both at orbital crossovers of the CryoSat-2 satellite and with coincident airborne observations of the sea ice freeboard. In Section 8 we discuss the theoretical limitations of the objective mapping technique and prospects for utilizing the method for multiple altimetry missions. Section 9 presents conclusions of the study.

2. Estimating Sea Surface Height in Sea Ice-Covered Locations

Satellite altimeter returns from leads within the sea ice pack are identified by their reflectivity and roughness, in the case of laser altimetry (Kwok, et al., 2007; Kwok, et al., 2019), or by their microwave scattering properties in the case of radar altimetry (Laxon, et al., 2003; Laxon, et al., 2013). The classification algorithms for identifying leads are generally based on thresholds of parameters for the returning laser or radar echo (Quartly, et al., 2019). These algorithms vary in complexity, depending on the number of parameters used, e.g. between 1 and 5+ (Ricker, et al., 2014; Wernecke & Kaleschke, 2015; Lee, et al., 2016; Meloni, et al., 2020), and can use machine learning for the training of thresholds (Lee, et al., 2016; Paul, et al., 2018). Alternative algorithms use, for instance, neural networks to classify echoes based on their shape (Poisson, et al., 2018). For CryoSat-2, returns from

leads typically make up 1 to 15% of all the valid samples (Wernecke & Kaleschke, 2015; Passaro, et al., 2018), with higher densities of returns in zones of first-year ice at the pack ice margins where the sea ice concentration is lower. The mean distance from a sea ice sample to the nearest lead along track is approximately 30 ± 60 km (based on our processing chain, see Section 3). However, interpolation distances for the SSH between lead samples actually depend on the 'strictness' of the waveform classifier, with a trade-off between the number of lead samples available and the precision/accuracy of those height observations. For instance, in the performance analysis of (Wernecke & Kaleschke, 2015) the most liberal classifier produced a lead sample density of 26% but included 13% false positive leads and high variance between proximal SSH observations. With the same dataset, a conservative classifier produced a sample density of only 1% but included zero false positives and low variance between observations.

Linear interpolation (Ricker, et al., 2014; Lee, et al., 2016; Landy, et al., 2017; Guerreiro, et al., 2017; Xia & Xie, 2018) or regression (Kwok, et al., 2007; Tilling, et al., 2018; Lawrence, et al., 2018) is used to estimate the SSH between lead tie-points (Fig. 1). A low-pass filter can be used to smooth the final surface at clusters of leads, where noise may introduce artificially rough sea surface topography. Data may be discarded where insufficient lead returns are available to reliably interpolate the SSH at a sea ice location (Tilling, et al., 2018). Uncertainty on the derived SSH is estimated from the root-mean square (RMS) height of lead returns within a moving window (25 km for instance) along track (Ricker, et al., 2014), or by analyzing the RMS of SSH pairs at orbital crossovers (Tilling, et al., 2018). For CryoSat-2, the uncertainty on a single SSH measurement has been estimated in the range of 2-50 cm. However, this uncertainty is likely to be correlated over wavelengths >100 km owing to the length-scale of the SSH interpolation, to the typical distances between lead observations and to errors in the satellite orbit determination or geophysical corrections (Wingham, et al., 2006). Consequently, random errors in the SSH observations in sea ice zones cannot simply be reduced by accumulating observations of the leads along the track.

In the current approach for estimating SSH from pulse-limited radar altimeters, significant positive biases can also be added to the radar range when leads located outside the nadir point of the satellite 'snag' the radar (Armitage & Davidson, 2014). This sea surface elevation bias ranges from -1 to -4 cm, depending closely on the strictness of the lead classification algorithm, and results in a 10-40 cm overestimate in sea ice thickness if uncorrected (Armitage & Davidson, 2014). The bias can be reliably removed by using information on the interferometric phase difference of the radar wave travel-time to

an off-nadir lead scatterer (Di Bella, et al., 2018; Di Bella, et al., 2020); however, of all the radar altimeters only the CryoSat-2 mission has had this capability, and only operating over a small part of the Arctic Ocean. Taking advantage of the interferometric SARIn-mode, around 35% of the lead returns discarded in SAR-mode can be retained, leading to a ~40% reduction in SSH uncertainty (Di Bella, et al., 2018).

3. Data & Preprocessing

3.1. CryoSat-2 Level 2 Processing

We use Baseline-C Level 1B CryoSat-2 waveform observations, details in (Bouffard, et al., 2018), for the period between October 2010 and April 2019 obtained from the official ESA science server (accessed in June 2019 at https://science-pds.cryosat.esa.int). SAR- and SARIn-mode observations are retracked by fitting waveforms to echoes simulated from a numerical model for the delay-Doppler SAR altimeter waveform (Landy, et al., 2019), using the Lognormal Altimeter Retracking Model (LARM) algorithm described in (Landy, et al., 2020). A local interpolation of the mean sea surface (MSS) is then removed from the profile of surface heights. The MSS model is a 10-km field obtained from the linear interpolation of all CryoSat-2 lead observations between 2010 and 2019. We apply a three-parameter classification routine to separate CryoSat-2 returns from sea ice and leads, based on the calibrated backscattering coefficient (σ^0), the pulse peakiness (PP) and the waveform stack standard deviation (Laxon, et al., 2013; Ricker, et al., 2014; Paul, et al., 2018), as described in (Landy, et al., 2020). Surface heights at leads referenced to the MSS, i.e. sea level anomaly (SLA) observations, are retained at this point for further analysis.

To obtain estimates for the radar freeboard, the long-wavelength (>200 km) median profile (which we assume contains residual error from the satellite orbital determination and/or geophysical corrections (Kwok & Cunningham, 2015) or largest-scale features of the dynamic ocean topography) is removed from each CryoSat-2 elevation track. SSH is estimated at sea ice locations by linear interpolation between lead tie-points (Landy, et al., 2017). We apply a 25-km low-pass filter to smooth sea surface topography at dense lead clusters and estimate the SSH uncertainty from the RMS height of leads within a 50 km window (Ricker, et al., 2014). Radar freeboard is then estimated from the sea ice floe elevation minus the SSH, and the 'single-shot' uncertainty on a freeboard measurement is the root-sum-square of the SSH uncertainty and speckle noise (which is 11.6 cm for SAR-mode and 15.3 cm for SARIn-mode (Wingham, et al., 2006)).

Furthermore, we use the SSH observations at leads within the sea ice pack to estimate monthly fields of the Arctic Ocean mean geostrophic current, following the method of (Armitage, et al., 2017). Dynamic ocean topography (DOT) within the sea ice-covered zone is estimated from the difference between CryoSat-2 SSH observations and the GOCO5S geoid (Kvas, et al., 2019), referenced to the same WGS-84 ellipsoid. The DOT therefore contains the long-term offset of the SLA with respect to the geoid. Estimates of the DOT greater than ±2 m are removed before the remaining estimates are sampled onto a 25-km Northern Hemisphere EASE2 grid and smoothed with a 300-km width Gaussian convolution filter. We calculate gradients of the smoothed DOT grid along zonal and meridional axes and convert these to u and v vectors of the surface geostrophic current following (Armitage, et al., 2017). For the purposes of this study, we calculate the average 'climatological' October-April Arctic Ocean surface current over the entire CryoSat-2 2010-2019 period and mask the region north of 87° latitude due to measurement noise (Fig. 2). The climatological field illustrates the major components of the long-term Arctic Ocean circulation in the winter, including the Beaufort Gyre, Transpolar Drift, East Greenland and Baffin Island currents, along with the Atlantic and Pacific inflows to the Arctic.

3.2. Airborne OIB Ku-Band Data Level 2 Processing

To validate the CryoSat-2 sea ice freeboard observations derived from our new method, we use geolocated Level 1B echograms from the Center for Remote Sensing of Ice Sheets (CReSIS) ultrawideband (UWB) Ku-band airborne radar altimeter, operated on Arctic campaigns by NASA Operation IceBridge (OIB), to generate airborne estimates of radar freeboard coinciding with the satellite. The data were accessed from https://data.cresis.ku.edu/#KBRA in January 2020. We selected five airborne campaigns in 2011, 2012 and 2014 (all in March) that were flown to coincide in space and time with CryoSat-2 overpasses and covered both first-year and multi-year sea ice in the Chukchi and Lincoln Seas, respectively. The CReSIS Ku-band radar has a central frequency of 15 GHz (Rodriguez-Morales, et al., 2013) and therefore should, in theory, produce a comparable estimate for the radar scattering horizon over snow-covered sea ice to the 13.6 GHz CryoSat-2 radar (Willatt, et al., 2011). The flat-surface range resolution of the UWB radar is approximately 4.9 cm in snow and the sensor has an along track sample spacing of approximately 5 m (Paden, et al., 2017).

Our processing methodology for the CReSIS radar is built on the algorithm detailed in (Landy, et al., 2020) to derive snow-ice interface elevation, with several additional steps required to determine the sea ice radar freeboard which we introduce here. We exclude all aircraft segments where the variability of the detrended aircraft altitude is >0.6 m, or where the mean aircraft pitch or roll is >6°. The local

CryoSat-2 MSS is removed from the retracked elevation profile. Radar returns from leads are classified by thresholding waveforms with σ^0 and PP above dynamic thresholds (Fig. 3a). Each threshold is determined from the 99th percentile of σ^0 or PP samples, but are no higher than 34 dB or 0.25, respectively, calculated recursively over groups of twelve radar segments (60 km total length). The SSH is estimated at ice floes using the method described in Section 3.1 and radar freeboard is obtained from ice floe elevations minus the SSH (Fig. 3b). We exclude all samples located more than 5 km from their nearest lead to prevent the introduction of correlated freeboard biases away from leads. A single airborne freeboard estimate is calculated per ~300 m coinciding CryoSat-2 footprint (Fig. 3b) following (Di Bella, et al., 2018).

3.3. Auxiliary data

The EUMETSAT Ocean and Sea Ice Satellite Application Facility (OSI SAF) global sea ice concentration climate data record (OSI-450) daily EASE2 gridded observations (accessed from ftp://osisaf.met.no/reprocessed/ice/conc/v2p0 in January 2020) (Lavergne, et al., 2019), are used to filter valid CryoSat-2 observations from the sea ice zone. The OSI SAF global sea ice type record (OSI-403-c) daily polar stereographic gridded observations (accessed from ftp://osisaf.met.no/archive/ice/type in June 2019) (Breivik, et al., 2012), are used to identify whether CryoSat-2 or OIB airborne observations are located over first-year or multi-year sea ice.

4. Correlation length scales for the Arctic sea level anomaly from satellite altimetry

To determine which leads can be used for interpolating the local SLA at sea ice floe locations, we must first define the typical spatial and temporal length scales of the Arctic SLA. The CryoSat-2 lead observations present several challenges for accurately resolving characteristic wavelengths of the SLA signal. Generally, the observations are strongly clustered into groups of 1-10 consecutive valid specular lead returns along the track. The distances between clusters of valid lead returns can also be in excess of 100 km along track, using our lead classification routine. Adjacent tracks are sampled every 1-2 hours and generally spaced hundreds of kilometers apart. Consequently, at small time and distance lags, we are limited by these sampling considerations and cannot accurately resolve the higher-frequency scales of the SLA. One might expect this to include SLA signatures of ocean circulation features (such as mesoscale eddies and meanders) caused by instability of ocean currents at the scale of the local, first-mode Rossby deformation radius, estimated to be around 5-15 km in the Arctic (Nurser & Bacon, 2014). These mesoscale features can alias the SLA signal, increasing the uncertainty in SLA

predicted for nearby leads. However, through the present analysis we will demonstrate that the Arctic Ocean SLA spatial decorrelation length scales are generally much larger than the local Rossby deformation radius.

Using CryoSat-2 observations for the Arctic SLA at leads within the sea ice pack, we map the winter decadal average spatial (in zonal and meridional directions) and temporal decorrelation length scales of the Arctic Ocean SLA signal. We map the length scales onto a 50 km EASE2 grid (Brodzik, et al., 2012) covering the Northern Hemisphere above 50 degrees latitude. We select a minimum lag distance of 2.5 km and lag time of 0.5 days based on the sampling limits of the CryoSat-2 data, although following our analysis the smallest scales identified were several times larger than these values. The covariance ρ of the SLA at lag distance or time r is defined as:

$$\rho(r) = \frac{1}{n(r) - 1} \sum_{i=1}^{n(r)} [z(x_i) - \bar{z}][z(x_i + r) - \bar{z}] \quad (1)$$

Where n is the number of paired observations at lag distance or time r, z is the instantaneous SLA, x_i is the location or time of observation i. The SLA signal is modelled with a Gaussian function, following previous studies in the equatorial oceans, e.g. (Jacobs, et al., 2001). This model can account for non-zero covariance between observation pairs within the few shortest lag bins, which we expect due to the uncorrelated speckle noise properties of 20 Hz CryoSat-2 observations, and asymptotic limit at the covariance amplitude, i.e. the random variance of the field. We fit the following Gaussian model to the empirical zonal, meridional, and time-dependent covariance functions obtained from Eq. (1):

$$\rho(r) = (a - s)e^{-\frac{3r^2}{L^2}} + s \quad (2)$$

Where a is the covariance amplitude, s is the covariance at r = 0, and $L/\sqrt{3}$ is the e-folding scale of the SLA. L is the 'effective range', which defines the lag where ρ drops to 5% of the covariance amplitude and is applied as the first zero-crossing of the imposed SLA signal decorrelation in Eq. 6 (Section 5). The model in Eq. (2) is fit to the empirical covariance functions with a bounded nonlinear least-squares optimization algorithm. The lower bound for s is zero and L is bounded at the maximum lag distance or time. The quality of fit is determined from the optimized coefficient of determination between empirical and model covariance functions.

4.1. Spatial and temporal length scales

To obtain spatial patterns for the characteristic SLA spatial length scale over the entire Arctic Ocean, we perform the following analysis at monthly intervals for the entire Oct-Apr 2010-2019 CryoSat-2 lead observation dataset. For every cell of the 50-km EASE2 grid we identify all SLA observations in the month within 500 km. Lag distances are employed at 5 km intervals from 2.5 to 502.5 km, including pairs from the same and different tracks. A time limit of 3 days between observation pairs is imposed to maximize the likelihood that observations are correlated in time (Pujol, et al., 2016) with sufficient observations remaining available for analysis. By doing this we are limiting the chances of decorrelation in time but searching for spatial correlations over a very wide range. The derived length scales are therefore representative of averaged conditions over a 3-day time window. We construct a matrix of the zonal and meridional distances of all valid observation pairs and sample the covariance for each lag bin along both directional axes using Eq. (1). We then fit the Gaussian model in Eq. (2) to each empirical function and determine the e-folding length, covariance amplitude and minimum covariance for the grid cell. Only grid cells with a model r^2 fit >0.3 are retained.

To determine the SLA temporal length scales, we again perform the following analysis at monthly intervals of the CryoSat-2 data. For every cell of the grid, we identify all SLA observations within 100 km and ±30 days of the 15th of the month. The spatial limit of only 100 km is chosen to maximize the likelihood that observations are correlated in space (Pujol, et al., 2016), with sufficient observations remaining available for analysis. By doing this we are limiting the chances of decorrelation in space but searching for temporal correlations over a very wide range. The derived time scales are therefore representative of averaged conditions over a 100 km radius. Since the orbit time for a single CryoSat-2 pass over the Arctic Ocean is a matter of minutes, we do not analyze the time-dependent correlation between SLA observations along the track. In contrast, we apply a low-pass median filter to observations within 100-km window clusters along the orbital track, to reduce the impact of small-scale signal noise along track on the time-dependent decorrelation of the SSH between tracks. Lag times are employed at 1-day intervals from 0.5 to 30.5 days. We construct a matrix of the time difference between all valid observation pairs and sample the covariance for each lag bin using Eq. (1). Applying Eq. (2) we then fit the Gaussian model to each empirical function and again determine the e-folding length, covariance amplitude and minimum covariance for the grid cell. Only grid cells with a model r^2 fit >0.3 are retained.

4.2. Mean decorrelation scales for the sea level anomaly

From the analysis of monthly-mean SLA covariance fields, we find no clear seasonal or interannual patterns in the variability of both the spatial and temporal correlation scales. Therefore, as a first estimate we calculate 2010-2019 'climatological' zonal, meridional, and temporal decorrelation length scales from the weighted mean of the e-folding lengths of all 62 fields (i.e., the total number of analyzed months), with the optimized model fit statistics providing the weights. We use these climatological scales for all remaining analysis. Another reason why climatological scales must be used is because there are typically too few lead observations proximal to sea ice samples from which to calculate local contemporary spatiotemporal correlation length scales, which can lead to high uncertainty in the derived SLA. Finally, we smooth the climatological fields with a 3 x 3 grid cell median filter to remove a few remaining anomalies.

The derived zonal, meridional, and temporal e-folding scales compare closely to the estimates of (Pujol, et al., 2016) obtained from multiple altimeter missions for sub-polar oceans. For example, (Pujol, et al., 2016) estimated zonal length scales of 45-100 km for the latitude band between 50 and 70 degrees north, which are comparable to our estimates of 40-120 km for the Arctic peripheral seas, the Barents, Kara, and Laptev Seas (Fig. 4a and b). Temporal scales (for the same latitude band) of 3-7 days (Pujol, et al., 2016) are marginally higher than our estimates from CryoSat-2 of 1-5 days for the peripheral seas (Fig. 4c). Our estimates for the zonal and meridional decorrelation scales (Fig. 4a and b) match patterns for the first-mode baroclinic Rossby radius obtained from hydrographic observations (Nurser & Bacon, 2014), with higher scales in the Western Arctic (Beaufort Sea region) than on the eastern side north of Svalbard (Fig. 4a and b). However, the CryoSat-2 e-folding scales of 50-200 km are an order-of-magnitude higher than the baroclinic deformation radius (see Section 4.4) supporting the sub-polar observations of (Chelton, et al., 2011). For instance, (Chelton, et al., 2011) show that eddies can be three times larger than the Rossby radius, suggesting that deformation radii cannot be directly associated with the size of eddies. Our CryoSat-2 data appear to characterize mesoscale anomalies at a scale between baroclinic instabilities and larger features of the geostrophic circulation field. However, the CryoSat-2 data do appear to resolve smaller 10s km features of the SLA signal over the shelf seas, for instance. The SLA decorrelation timescales (Fig. 4c) match the typical 1-7 day synoptic period of passing weather systems (Hutchings, et al., 2011).

Variations in the characteristic spatial and temporal length scales of the SLA are controlled by the Arctic Ocean's bathymetry, with shallower bathymetry on the shelves introducing additional tidal signals to the SSH that may be uncorrected and cause the signal to decorrelate more rapidly (Armitage,

et al., 2017). Generally, the patterns of the zonal and meridional length scales are quite similar, although it is particularly evident in the Siberian Seas and also in Hudson Bay and the Greenland Sea that the meridional scale is significantly shorter than the zonal scale (Fig. 4a and b). This makes sense as the SSH will be less well correlated across the shelf-break than along it and emphasizes the need to apply these two scales independently in the analyses below. It is also interesting that the space and time decorrelation scales appear to be considerably longer in regions covered by ice for most of the year (i.e. the perennial ice zone) than areas of the marginal ice zone (MIZ) with lower sea ice concentrations.

The covariance amplitude (Fig. 5a) characterizes the standard deviation of the SLA outside the correlation timescale shown in Figure 4c, i.e. the variability present in the SSH signal over long time periods. It ranges from approximately 6 cm over the Central Arctic Ocean to 15+ cm on the shelf seas. If the SSH is estimated at a location from leads exclusively outside the correlated zone, the uncertainty on the SSH estimate can be no better than this value, which is a salient point because the conventional methods for interpolating SLA (Section 2) have often used length scales well above those shown in Figure 4. The covariance at zero lag ranges from around 2 cm over the central ocean to 6 cm on the shelf seas (Fig. 5b). These values represent the characteristic uncertainty on an estimate for the SSH using only lead observations in the immediate vicinity of a location and close in time, from all available tracks. Generally, this includes only a small number of lead observations but with a low sample variance, and the Arctic Ocean mean of 3.8 cm is similar to the estimate of ~4 cm SSH uncertainty derived from orbit crossover analysis (Tilling, et al., 2018).

4.3. Interpreting the decorrelation scales

We can expect the ocean surface to be 'flat' over a length scale defined by the first mode baroclinic Rossby radius of vertical deformation, which characterizes the approximate scale of boundary currents, eddies, and fronts. In the weakly-stratified Arctic Ocean and shallow shelf seas, the baroclinic Rossby radius has been determined as only 2-16 km from a climatology of hydrographic observations (Nurser & Bacon, 2014). This is around an order-of-magnitude smaller than the length scales over which SLA is conventionally interpolated along the altimeter's orbital track when deriving sea ice freeboard (see Section 2). Therefore, small-scale dynamic features of the ice-covered Arctic Ocean surface topography cannot reliably be resolved from dispersed lead observations in along-track altimeter data (let alone in adjacent time-lagged tracks). However, sea ice floes can interact with and suppress dynamic features such as eddies (Meneghello, et al., 2017), so the SLA in ice-covered waters may – in

reality – covary over much longer distances than the baroclinic Rossby radius predicts (Chelton, et al., 2011; Nurser & Bacon, 2014).

To examine whether this is likely to be the case, we have further analyzed the covariance of SSH fields from a 1/12° global simulation (the ORCA0083-N06 run) of the coupled ocean-sea ice model OPA-LIM2 (Madec, et al., 1998; Fichefet & Morales Maqueda, 1997; Goosse & Fichefet, 1999), applying an identical method to the one we applied here for CryoSat-2 (Fig. S3) every 5 days between 2011 and 2015. The model uses the quasi-uniform, tri-polar ORCA grid (Madec & Imbard, 1996) to avoid the singularity associated with convergence of meridians at the north pole. The grid has 75 vertical levels and a lateral resolution of 2-5 km in the Arctic region (Fig. S1), which should be sufficient to capture decorrelation length scales of the SLA of order 10s km, indicative of dynamic features (such as eddies, e.g. see Fig. S2) that we may be missing with CryoSat-2. The uniform model SSH fields also do not suffer from the same nonuniform clustered sampling limitations of the altimeter data. This configuration of NEMO has been widely used for Arctic Ocean studies, e.g. (Bacon, et al., 2015; Tsubouchi, et al., 2018; Kelly, et al., 2019). The SLA is calculated from the SSH fields with reference to a mean sea surface height model derived from all time slices between 2011 and 2015.

We find the smallest e-folding length scales from NEMO are 10-20 km in the North Atlantic (Fig. S4, which suggests the model can resolve small-scale dynamical features if they are present. Patterns of the zonal and meridional length scales are remarkably similar to CryoSat-2, with the largest scales in the Central Arctic and much smaller scales in the sub-polar seas. The range of length scales between NEMO and CryoSat-2, of around 20-200 km, are almost identical. There are relatively higher length scales in the East Siberian Sea, Central Arctic and Hudson Bay, and relatively lower scales in the Southern Beaufort Sea and Baffin Bay, between NEMO and the CryoSat-2 data. These model findings support previous idealized simulations of the Beaufort Gyre that resulted in eddies emerging with about 100 km scale (Manucharyan & Spall, 2016). Large-scale variability can still dominate the SLA due to basin and gyre scale mechanisms that exaggerate the correlation lengths (Jacobs, et al., 2001). To examine whether our CryoSat-2 observations may be picking up only the largest gyre-scale features of the SSH, we try low-pass filtering the NEMO SLA to remove features greater than 250 and 125 km and recalculating the length scales (Fig. S5). Even after removing features >125 km, the derived scales remain 20-100 km within the Arctic and do not reduce to Rossby-like radii (despite these decorrelation scales appearing at other locations, such as the North Atlantic where the model grid is actually coarsest). This implies that length scales obtained from our analysis of the NEMO and CryoSat-2 data without filtering are the dominant length scales of the SLA.

The covariance amplitudes of the NEMO SLA also has a similar pattern to those derived from CryoSat-2 (Fig. S4) but are consistently ~5 cm lower reflecting the absence of measurement noise in model SSH fields. The NEMO amplitudes also underestimate the high CryoSat-2 amplitudes measured in Hudson Bay and the Canadian Arctic, for example. One final notable result from the NEMO analysis is that length scales are almost always higher when a grid cell is ice-covered than ice-free. Presence of sea ice reduces covariance amplitudes by 65% and increases decorrelation scales by 20% on average when we test the same locations with and without sea ice (Fig. S6). This may partly explain the enhanced decorrelation scales measured by CryoSat-2 in the perennially ice-covered Central and Western Arctic.

The apparent decorrelation length and time scales observed by CryoSat-2 are also supported by previous observations of sea ice motion from ice-mounted buoy arrays. Multi-scale drifter arrays deployed in the Beaufort Sea as part of the 2007 SEDNA experiment showed little coherence in ice deformation patterns across spatial scales of 10-100 km, with coherence only appearing at scales exceeding 100 km (Hutchings, et al., 2011). The observed coherence between buoys is also typically only lost over synoptic time periods longer than 3-8 days (Hutchings, et al., 2011). These evident spatial scales of coherent sea ice motion are >10 times larger than the first mode baroclinic Rossby radius of deformation, reflecting more closely the apparent decorrelation scales of the SSH signal observed by CryoSat-2 (Figure 4). For example, we find characteristic scales for the SSH signal of 100-150 km and 2-5 days in the Beaufort Sea.

5. Objective mapping for estimating the SLA at sea ice floes

We use an objective mapping methodology to estimate the instantaneous sea level anomaly at all sea ice floe locations along the CryoSat-2 altimeter track. The method is a suboptimal space-time objective analysis based on the Gauss-Markov theorem (Le Traon, et al., 1998) that takes into account both random uncorrelated errors of the altimeter range measurement (e.g. speckle noise) and long-wavelength along-track correlated errors such as those related to the satellite orbit or L1B tidal corrections (Wingham, et al., 2006). The SLA is obtained at any location from the best linear estimate of a given irregularly distributed sample of CryoSat-2 SLA observations at proximal leads (on the orbital track in focus and adjacent tracks), their errors, and an assumed covariance function of the SLA space-time signal.

The best least-squares linear estimator θ_{est} and associated error field ϵ^2 for the *a priori* unknown sea level anomaly at a sea ice floe location are (Le Traon, et al., 1998; Ducet, et al., 2000; Pujol, et al., 2016):

$$\theta_{est} = \sum_{i=1}^{n}\sum_{j=1}^{n} A_{ij}^{-1} C_{xj} \Phi_{obs} \tag{3}$$

$$\epsilon^2 = C_{xx} - \sum_{i=1}^{n}\sum_{j=1}^{n} C_{xi} C_{xj} A_{ij}^{-1} \tag{4}$$

Where Φ_{obs} is an observation, i.e. the true SLA Φ_i and its observation error ε_i. $\boldsymbol{A}$ is the covariance matrix of all n selected observations, and $\boldsymbol{C}$ is the covariance vector between the observations and field to be estimated:

$$\begin{aligned} A_{ij} &= \langle \Phi_{obs} \Phi_{obs} \rangle = \langle \Phi_i \Phi_j \rangle + \langle \varepsilon_i \varepsilon_j \rangle \\ C_{xi} &= \langle \theta(x) \Phi_{obs} \rangle = \langle \theta(x) \varepsilon_i \rangle \end{aligned} \tag{5}$$

Where $\theta(x)$ is the SLA at the ice floe location x. The zonal, meridional, and temporal decorrelation scales and propagation velocities characteristic of the SSH signal to be retrieved are defined by the covariance function (Arhan & De Verdiére, 1985):

$$\begin{aligned} C(r,t) &= \left[1 + ar + \frac{1}{6}(ar)^2 - \frac{1}{6}(ar)^3\right] e^{-ar} e^{-\frac{t^2}{T^2}} \\ a &= 3.337 \\ r &= \sqrt{\left(\frac{dx - P_x dt}{L_x}\right)^2 + \left(\frac{dy - P_y dt}{L_y}\right)^2} \end{aligned} \tag{6}$$

dx, dy and dt are the distance in space (zonal and meridional directions) and time to the observation or estimator location under consideration, L_x, L_y and T are the zonal, meridional, and temporal decorrelation length scales defined by the effective range in Eq. (2) (Section 4.3), and P_x and P_y are propagation velocities of the SSH signal in zonal and meridional directions (Section 3.1). We use the long-term average propagation velocities, obtained from the climatological geostrophic currents (Figure 2), for P_x and P_y. This covariance function has been regularly applied to model the SSH signal in sub-polar seas (Le Traon, et al., 1998; Le Traon, et al., 2003; Pujol, et al., 2016) and its properties are illustrated in Figure 6. The observation errors have two components: an uncorrelated random component with variance b^2 which contributes to the diagonal of the $\langle \varepsilon_i \varepsilon_j \rangle$ matrix and a long-wavelength correlated component E_{LW}. The latter is added to non-diagonal terms of the $\langle \varepsilon_i \varepsilon_j \rangle$ matrix as $\delta_{ij} b^2 + E_{LW}$ if observations i and j are on the same track, where δ_{ij} is the Kronecker delta. The field ϵ^2 is expressed as a fraction of the error variance, so a final estimate for the total SSH uncertainty θ_{unc} is obtained from:

$$\theta_{unc} = \sqrt{\epsilon^2 b^2} \quad (7)$$

Which can be related directly to estimates for the sea level uncertainty at sea ice floes obtained through conventional methods, such as from the root-mean square of lead elevations within a defined window along the altimeter track.

For each CryoSat-2 return classified as a sea ice floe along track, we first sample the zonal, meridional, and temporal decorrelation length scales, and geostrophic currents, from the mean fields shown in Figures 1 and 3 at this 'estimator location'. We identify all available SSH observations (leads) within three times the spatial and temporal correlation scales from this location, including observations both on and off the estimator track. However, only one of four observations is retained outside one correlation length to reduce the size of the matrix inversion, i.e. (Pujol, et al., 2016). The number of valid observations meeting these criteria can still exceed 10,000 for locations close to the pole. Therefore, we determine the covariance vector between all observations and the estimator location using Eq. 6 and retain only N points with highest absolute correlation $|C|$. Increasing N theoretically improves the accuracy of the retrieved SSH and reduces the uncertainty, but we use N = 2001 hereafter for this study in order to limit the size of the matrix to be inverted in Eq. 3. One month of CryoSat-2 Arctic Ocean observations takes approximately four days to process on a 56 core 256 GB RAM cluster with this criterion.

The covariance matrix in Eq. 5 is constructed between all SLA observations. The 'single-shot' random error b associated with a 20 Hz CryoSat-2 observation is 11.6 cm for SAR mode and 15.3 cm for SARIn mode (Wingham, et al., 2006). This is combined with the long-wavelength error E_{LW} estimated as 25% of the signal variance $E_{LW} = 0.25Var(\Phi_{obs})$, based on results from previous studies (Le Traon, et al., 1998; Ducet, et al., 2000; Le Traon, et al., 2003), to construct the error matrix in Eq. 5. An optimal estimate for the SLA at the sea ice floe is then obtained from the integrated inverse sum of the observation covariance and error matrices, through Eq. (3), and the SSH uncertainty is obtained from Eqs. (4) and (7). Finally, after deriving individual SLA estimates for every CryoSat-2 footprint classified as sea ice along a track, we smooth the resulting profile with a low-pass filter whose window is limited to the mean of the local SSH e-folding scales $\frac{(L_x+L_y)}{2\sqrt{3}}$. This removes noise introduced by anomalous leads for a few samples.

6. Results from March 2013

We compare our results obtained for the SLA at sea ice floes with a conventional method and the new objective mapping approach for March 2013. The conventional method applied uses the external DTU18 MSS model for deriving SLA, linear interpolation between leads along track, smoothed with a low-pass filter, with the SSH uncertainty obtained from the RMS height of leads within a 25-km moving window along track (Landy, et al., 2017).

6.1. Case study track on March 3rd

We first select a single ascending-orbit CryoSat-2 SAR-mode track at 03:46:51 on 3rd March 2013 to illustrate the advantages of the new method. This track crosses the Arctic Ocean from the Lincoln Sea to the East Siberian Sea. Although the Eastern Arctic sector of the track contains dense lead clusters, our waveform classification algorithm produces only five valid lead returns for the remaining 1800 km (Fig. 7a). This track represents a case with particularly low lead density and requires interpolation of the SLA over distances of up to 500 km to ice floes from their nearest lead (if all floes are to be included in the analysis). Owing to the low lead density, uncertainty on the derived SLA is >6 cm for the majority of the track (Fig. 7a), representing 20-50% of the final derived radar freeboard (Fig. 7d). In areas with sparse leads, the estimated SLA can be tied to single lead observations (Fig. 7a) despite each observation having a random uncertainty up to ~15 cm (Wingham, et al., 2006) and possible bias >4 cm (Armitage & Davidson, 2014).

By applying the objective mapping approach, we sample up to 2001 local observations at leads for every sea ice floe along track and estimate the SLA from the optimal interpolation of them all. Figure 7b illustrates the covariance between the location of every 80th sea ice floe along track and its local sample of SSH observations. Generally, the SLA of the distribution of lead observations around a single ice floe ranges from approximately -0.2 to +0.2 m but is higher in the shallower East Siberian Sea sector (1800-2500 km along profile). For this track, 56% of all SLA observations used in the analysis are within half the distance of both L_x and L_y correlation length scales and 83% of observations are within the whole distance of L_x and L_y.

The final optimal interpolation (Fig. 7c) predictably coincides with most of the lead observations on the focus track because they have a time lag close to zero. However, the covariance matrix between the up to 2001 neighboring lead observations in a local sample provides a weighting on the SLA estimate that reduces the influence of anomalous observations, i.e., leads with high estimated measurement error with respect to their neighbors. For instance, the objective SLA estimate is 5 cm lower than the lead at *(i)* in Figure 7c, indicating this SLA observation may contain significant error. Single isolated leads or

lead clusters do not over-influence the objective SLA estimate (Fig. 7c) in the same way they can for the conventional method (Fig. 7a). In such instances where the objective analysis indicates a lead is under- or over-estimated, as it does at *(i)*, the derived radar freeboards between the new and conventional approaches contain long wavelength correlated offsets, typically of between -20 and +20 cm (Fig. 7d). The uncertainty estimate for the objective analysis (from Eq. 7) is generally <2 cm, representing <15% of the final derived radar freeboard (Fig. 7d), because the SLA is estimated from tens-to-hundreds of times more observations than in the conventional approach (Fig. 7c). The uncertainty is notably higher at *(ii)* in Figure 7c because L_x and L_y are <150 km at this location, so the number of available SLA observations is significantly lower than the maximum 2001 permitted and their variance is larger (Fig. 7b).

The new scheme for determining SLA enables the radar freeboard to contain greater along-track variability than the conventional scheme (Fig. 7d) because the estimated SLA is not fixed over long (>100 km) distances along track by isolated single or clusters of leads. The new scheme appears to be particularly successful resolving discontinuities in SLA (and its uncertainty) at the shelf break and other areas of complex bathymetry. For instance, the SLA does not become aliased when there are insufficient leads to resolve the detailed ocean surface topography, e.g., at *(iii)* in Fig. 7a and c.

6.2. Analysis of entire month

We complete the same comparison between the conventional SLA estimated from a linear interpolation along-track and from the objective analysis of all proximal leads from adjacent tracks, for every CryoSat-2 SAR and SARIn mode track in March 2013. Pairwise differences in the radar freeboard obtained from the conventional and objective methods are normally distributed (Fig. 8a and b) but comprise long-wavelength (10-500 km) correlated offsets between the methods in either direction. (Note we do not discard any freeboard observations based on their distance to the nearest along-track lead for this analysis). The radar freeboards can diverge by >5 cm along large segments of individual tracks (Fig. 8a), where the conventional SLA estimate is poorly constrained through biased observations or a low density of lead observations along track (Section 6.1). The conventional method is essentially as likely to underestimate the objectively mapped SLA as overestimate it (Fig. 8a). On average, the conventional method underestimates the objective mapping method by ~1 cm (Fig. 8b), constituting an estimated sea ice thickness difference of only ~10 cm. However, the mean absolute radar freeboard difference is 3.3 cm, which represents a 27% local uncertainty on the mean freeboard and constitutes >30 cm uncertainty in sea ice thickness estimated from these freeboards. The biases

between SSH mapping techniques appear to be independent of location, although there is a pattern of positive freeboard differences (mean = +2.5 cm) in the multi-year ice zone north of Canada and the largest differences are evident in coastal regions (Fig. 8a). These areas coincide with shallower tidal zones that have high SLA variability over short temporal and spatial scales (e.g. Fig. 5) and/or have the lowest available density of SSH observations at leads (Wernecke & Kaleschke, 2015).

By utilizing many times (typically 1-2 orders-of-magnitude) more SSH observations to determine the optimal SSH at a sea ice floe, the objective mapping method produces a factor of three reduction in the estimated SSH uncertainty (Fig. 8c). The objective analysis accounts for uncorrelated random errors in the observations, as well as long-wavelength correlated errors along the altimeter's orbital track caused by observation biases or errors in the orbit determination or geophysical corrections. Their reduction to the error estimate at a single ice floe scales directly with the number of observations and tracks, weighted by the covariance of the observations to the floe location and the covariance matrix between neighbors (Section 5). This objective estimate for the uncertainty is therefore based entirely on the observations themselves and does not suffer from the assumptions or conditions of the conventional method, for instance that the SSH uncertainty is uniform across the Arctic or depends only on the RMS of SSH observations along track (Section 2).

7. Validation of SLA and radar freeboard estimates

7.1. Analysis at orbital crossovers

As a first assessment of the precision of the new objective mapping method for deriving SLA at ice floes we identify all crossovers of the CryoSat-2 orbit over the Arctic Ocean sea ice pack in March 2013. Around 13,000 unique crossovers are identified where orbits intersect within 24 hours and valid CryoSat-2 measurements for each track are no more than 5 km apart. The crossover locations are clustered around the north pole, because the polar-orbiting satellite disproportionally crosses itself within a small region north of ~84 degrees latitude; however, there are rings of crossovers at around 66 and 79 degrees too (Fig. 9c).

All pairwise differences in the SLA or radar freeboard estimated at crossover locations are normally distributed (Fig. 9). The widths of the distributions represent a combination of random noise in the measurements, orthogonal sensing footprints for crossing orbits, aliased tidal signals, and – in the case of the radar freeboards – additional errors relating to ice motion and possibly radar signal penetration e.g. (Willatt, et al., 2011). The new objective mapping scheme reduces the RMS of the SSH estimated

at crossover locations by 70% compared to the conventional approach, from 4.6 down to 1.4 cm (Fig. 9a). The RMS of crossovers for the conventional scheme is close to the 4 cm reported by (Tilling, et al., 2018). It is not surprising that the RMS is reduced through objective analysis, as the SSH is estimated at ice floes from all available leads on all proximal tracks. However, with our new scheme the SSH compared at a crossover is still, in all cases, from an optimal interpolation of nearby observations rather than actual lead observations, so the improvement remains impressive. The objective mapping scheme reduces the RMS of the radar freeboard measured at crossover locations by 19% compared to the conventional approach, from 6.9 down to 5.5 cm (Fig. 9b). The improved SSH estimation reduces a portion of the radar freeboard uncertainty. However, because the new scheme reduces the RMS of radar freeboard at crossovers by significantly less than it reduces the RMS of SSH at crossovers, this suggests around three quarters of the total uncertainty in freeboard measurements at crossovers is ice-related (i.e. including the effects of ice motion, signal penetration, speckle noise and retracking uncertainties).

7.2. Independent validation of radar freeboards

We use independent radar freeboards derived from the CReSIS airborne Ku-band radar flown on OIB Arctic campaigns (Section 3.2) to compare the accuracies of the conventional and objective SSH mapping techniques. The Ku-band radar freeboards are used here rather than the official OIB L4 total (snow plus sea ice) freeboard and thickness product, so that we do not have to correct freeboards for snow depth and delayed radar wave propagation through the snow layer (Landy, et al., 2020). The OIB L4 snow depths contain known biases (Newman, et al., 2014) and fixed snow densities may introduce further systematic uncertainties (Mallett, et al., 2020). So, we use airborne radar freeboards to mimic the CryoSat-2 radar measurements as closely as possible and limit the chances of introducing further systematic biases into our comparisons. Satellite radar freeboards are obtained with both the objective and conventional SSH interpolation methods along CryoSat-2 tracks coinciding with five processed OIB campaigns in 2011, 2012 and 2014. Of the five coinciding tracks, three produced similar radar freeboard profiles between the objective and conventional methods suggesting that the conventional along-track approach was sufficient to resolve the SSH in these cases. The more sophisticated but less computationally efficient objective analysis is not always necessary. However, for two of the campaigns, on 26th March 2012 (CryoSat-2 in SARIn mode, with a 1-hour time difference between aircraft and satellite passes) and on 26th March 2014 (SAR mode, with a 4.5-hour time difference), satellite radar freeboards from the objective analysis and conventional approaches diverged

significantly. Here, we want to analyze which, if either, method accurately reproduces the airborne radar freeboards.

The OIB campaign on 26th March 2012 measured mostly multi-year sea ice with some first-year ice in the 'Wingham Box' (Fig. 10). The SSH estimated for this track with objective analysis was between 4 and 10 cm lower (Fig. 10a) than the SSH estimated with the conventional along-track approach but, owing to a low density of leads in the region, both methods included a relatively high uncertainty estimate (Fig. 10b). (Note the uncertainty in Figure 10a and b characterizes the precision of the estimated SSH, whereas the remaining analysis here characterizes its accuracy). Figure 10c illustrates the airborne and two satellite radar freeboard profiles, after a moving average filter with 2 km width is applied. There is some correlation between the airborne and satellite observations in places, but it is very clear that the distribution of radar freeboards from the objective mapping method matches the airborne observations far better than the distribution obtained from the conventional along-track method (Fig. 10d and e). The conventional method appears to underestimate the airborne freeboards by 8.9 cm (mean difference, MD), because it overestimates the SSH (Fig. 10b). In comparison, the MD between the objectively mapped CryoSat-2 freeboards and OIB is -3.4 cm. The accuracy of the new method (RMSE = 11.2 cm) is improved by around 25% versus OIB relative to the conventional method (RMSE = 14.9 cm), at the 2-km length-scale of our averaged freeboard observations.

The OIB campaign on 26th March 2014 measured predominantly multi-year ice in the Lincoln Sea (Fig. 11). The SSH estimated for this track with objective analysis was between 0 and 8 cm lower (Fig. 11a) than the SSH estimated with the conventional along-track approach and both methods produced lower uncertainty estimates at one end of the section, owing to a cluster of leads to the north (Fig. 11b). Figure 11c illustrates the airborne and two satellite radar freeboard profiles, after a moving average filter with 2 km width is applied. Like in the 2012 comparison, the CryoSat-2 freeboards from each method exhibit long-wavelength (>100 km) correlated differences (Fig. 11b). Again, it is clear that the distribution of radar freeboards from the objective mapping method match the airborne observations better than the distribution obtained from along-track interpolation between leads (Fig. 11d and e). The conventional method underestimates radar freeboard by MD = 11.1 cm, in comparison to 4.8 cm for the new method. The accuracy of the objective mapping method (RMSE = 13.8 cm) is improved by around 20% versus OIB relative to the conventional method (RMSE = 17.1 cm), at the 2-km length-scale of our averaged freeboard observations.

Our independent evaluation of the CryoSat-2 radar freeboards for both OIB campaigns demonstrates that long-wavelength errors, caused for example by a low density of valid lead returns along track, off-nadir lead errors, or errors in the L1B CryoSat-2 orbital/geophysical corrections, can introduce significant biases into derived radar freeboards using the conventional SSH mapping approach. In both cases where the conventional and objective SSH mapping techniques diverged, the objective estimate more accurately reproduced the radar freeboards observed from OIB aircraft observations.

8. Discussion

8.1. Prospects for further improvement

There are several avenues worth exploring to further improve the objective mapping of SSH in ice-covered seas. It may be valuable to use leads at adjacent tracks for mapping SLA at ice floes with ICESat-2, because regions of sea ice further than 10 km from their nearest lead reference along track are currently discarded (Kwok, et al., 2019). This leaves some areas such as the densely-concentrated multi-year ice of the Central Arctic occasionally missing valid observations e.g., (Petty, et al., 2020). However, the higher density of SSH observations from ICESat-2 may enable an improved characterization of the spatiotemporal characteristics of the SLA signal, and possibly also its seasonal variation, for other altimetry missions. It may also enable discarded ICESat-2 segments in lead-sparse regions like the Canadian Arctic Archipelago or Lincoln Sea to be retained (Kwok, et al., 2019). Now that Sentinel-3A and -3B are operating together with CryoSat-2 over a portion of the Arctic Ocean (Lawrence, et al., 2019), there is strong potential for characterizing the SLA signal in more detail combining all three sensors. Moreover, CryoSat-2 has been maneuvered to coincide more frequently with the ground track of ICESat-2 (as part of the *CRYO2ICE* Project) which could enable the direct intercomparison of SLA characteristics.

It is unlikely our assumption that systematic error between altimeter tracks is a maximum 25% of the signal variance holds in all situations (Section 5). The systematic offset between tracks will be greater when (i) orbital errors are higher (Wingham, et al., 2006), (ii) geophysical corrections for tides and atmospheric effects are lower quality or aliased by the satellite orbit, and/or (iii) target-dependent biases such as the snagging of off-nadir leads (Di Bella, et al., 2018) or variable radar penetration depths into snow e.g. (Willatt, et al., 2011) are greater. The objective SLA mapping results would be improved if the long-wavelength correlated component E_{LW} in Eq. (5) was determined from these error contributions or their spatiotemporal variability.

Finally, our current implementation of the objective mapping scheme takes approximately five days to process one month of CryoSat-2 SLA estimates at ice floes over the Arctic Ocean. This is around 3-4 orders-of-magnitude longer than conventional along-track SSH interpolation methods. However, it may be possible to obtain results with similar accuracy but only processing one in n sea ice floe samples along track, or using a reduced sample size of SSH observations, with considerable improvements in computation speed. Equivalent results may also be possible but using faster and less data intensive optimization algorithms.

8.2. Implications of the new method for deriving inter-mission data products and to the reanalysis of historic altimeter missions

The depth of snow on Arctic sea ice has been estimated from the offset between laser freeboards from ICESat-2 (Kwok, et al., 2020) or radar freeboards from the Ka-band AltiKa (Lawrence, et al., 2018) and radar freeboards from CryoSat-2. Whilst we do not expect errors in the determination of SLA to introduce pan-Arctic uniform biases between satellites (Fig.7b), the along-track correlated errors from interpolation between leads (Fig. 7a) could realistically introduce local biases to the derived inter-mission snow depths. These biases may either amplify or cancel each other out. Objective mapping therefore offers the prospect of combining SSH observations from multiple altimeter missions (Le Traon, et al., 2003; Pujol, et al., 2016): calculating constant inter-mission biases if present but, more importantly, preventing local biases where leads are sparse or have high uncertainty. Errors will be limited at mission crossover locations (Fig. 9) and systematic uncertainties should also be reduced on gridded freeboard differences.

The objective SLA mapping scheme offers most improvement over conventional techniques where sea ice concentrations are highest and/or SLA observations at leads have largest height uncertainty. For instance, the most obvious changes in gridded freeboard in Figure 8a occur in the perennially-ice covered zone north of Greenland and Canada. Historic pulse-limited radar altimeter missions, such as Envisat or ERS-1 and -2 (and the ongoing mission AltiKa), have an effective footprint of 2-8 km and are therefore more sensitive to ‘snagging’ than the SAR-focused CryoSat-2 (Section 2). The instruments on ERS-1/-2 also had a larger bandwidth than recent missions, meaning their range resolution was lower with specular lead reflections more likely to be aliased in the recorded waveforms. By estimating the optimal local SLA from a greater number of proximal lead observations, accumulated from multiple tracks, our new scheme should effectively reduce the random uncertainty from noise and waveform aliasing and the systematic uncertainty from snagging. Since a higher

number of leads are used for each SLA interpolation, a more conservative lead classification can be employed for a smaller sample of higher accuracy SLA observations. Improvements on the conventional SLA interpolation schemes for these missions should, in theory, be larger than we have found for CryoSat-2.

9. Conclusions

The conventional method for estimating sea ice freeboard with altimetry uses only lead observations along the satellite orbital track to interpolate the local sea surface height at ice floes. The SSH uncertainty is typically estimated from the root-mean-square of lead height observations within a moving window along track. Here we have introduced a new method to determine the optimal interpolation of local SLA at sea ice floes using all valid proximal lead observations both on the orbital track in focus and other adjacent tracks. The objective mapping method assumes that spatial and temporal properties of the SLA in ice-covered waters can be predicted with a characteristic Gaussian covariance function. The decorrelation length scales and signal propagation velocities that constrain this function in the Arctic Ocean are obtained by analyzing historic SLA measurements acquired by the CryoSat-2 radar altimeter from lead locations between 2010 and 2019. The best linear least-squares solution for the SLA at each ice floe is determined from all valid SLA observations, weighted by their covariance with the floe location, their covariance with neighbors (i.e. to identify anomalies), and their random and systematic observation errors.

By exploiting a greater number of leads for interpolating the SLA, it is possible to use a stricter pulse peakiness classification threshold – discarding more ambiguous lead waveforms without compromising the height estimate and its uncertainty. For instance, the objective mapping method can effectively reduce off-nadir lead biases on the derived CryoSat-2 SLA when corrections from the interferometric phase are not available. Applying the new method to the Arctic Ocean in March 2013, our results demonstrate that the SSH uncertainty can be reduced by around three times in comparison to conventional uncertainty estimates. The root-mean square of interpolated SSH pairs at orbital crossovers is reduced by a factor of three and radar freeboard crossover RMS is reduced by 20%. Where independent airborne observations are available and the coinciding new and conventional SSH estimates from CryoSat-2 give different results, we find the objective method improves satellite-derived freeboard accuracy by 20-25%. The new method is also capable of resolving much finer-scale detail of the SSH signal in areas of complex ocean topography such as the circumpolar shelf break. However, inversion of the SSH observation matrix is computationally expensive, so our current

742 software takes around five days on a cluster to process SSH at ice floes for one month of pan-Arctic
743 CryoSat-2 data.

744 Objective SSH mapping produces the largest improvements at local scales and may therefore enable
745 accurate sea ice freeboards to be estimated at kilometer-scale resolutions along the satellite track. With
746 CryoSat-2 maneuvered to align with ICESat-2 from August 2020, it will be valuable to inter-compare
747 the SSH between these two satellites and test whether objective mapping can reduce local biases in the
748 freeboard offsets. Furthermore, the scheme offers considerable potential for new missions such as
749 CRISTAL and for reprocessing ice freeboards from historic pulse-limited radar altimetry missions,
750 including AltiKa, Envisat, ERS-1 and -2, where SSH observations are more likely to have off-nadir
751 lead biases, higher noise and are regularly spaced >100 km along track.

752

Acknowledgements

The authors would like to thank the European Space Agency for pre-processing the CryoSat-2 observations to waveform Level 1B. JL acknowledges support from the European Space Agency Living Planet Fellowship "Arctic-SummIT" under Grant ESA/4000125582/18/I-NS. MT, JL, YA and SR acknowledge support from the Natural Environment Research Council Project "PRE-MELT" under Grant NE/T000546/1. JL acknowledges the "Diatom-ARCTIC" project (NE/R012849/1) and CW acknowledges the "APEAR" project (NE/R012865/1, NE/R012865/2), part of the Changing Arctic Ocean programme, jointly funded by the UKRI Natural Environment Research Council (NERC) and the German Federal Ministry of Education and Research (BMBF). MT acknowledges support from ESA's "CryoSat+ Antarctic Ocean" under grant ESA AO/1-9156/17/I-BG and "EXPRO+ Snow" under grant ESA AO/1-10061/19/I-EF. We acknowledge the use of data and/or data products from CReSIS generated with support from the University of Kansas, NASA Operation IceBridge grant NNX16AH54G, NSF grants ACI-1443054, OPP-1739003, and IIS-1838230, Lilly Endowment Incorporated, and Indiana METACyt Initiative. This work used the ARCHER UK National Supercomputing Service (http://www.archer.ac.uk) for producing NEMO model simulations. We thank Andrew Coward for developing and running the NEMO model experiments and George Nurser for providing global fields for the baroclinic Rossby radius from (Nurser & Bacon, 2014). The along-track CryoSat-2 observations of SSH for 2011-2019 are available by request from the authors. Gridded CryoSat-2 Baseline-C radar freeboards from the LARM algorithm are freely available at the UK Polar Data Centre *https://data.bas.ac.uk/full-record.php?id=GB/NERC/BAS/PDC/01257*.

References

Aksenov, Y. et al., 2017. On the future navigability of Arctic sea routes: High-resolution projections of the Arctic Ocean and sea ice. *J. Marine Policy*, Volume 75, pp. 300-317.

Allard, R. et al., 2018. Utilizing CryoSat-2 Sea Ice Thickness to Initialize a Coupled Ice-Ocean Modeling System. *Adv. Space Res.*, 62(6), pp. 1265-1280.

Arhan, M. & De Verdiére, A., 1985. Dynamics of eddy motions in the eastern North Atlantic. *J. Phys. Oceano.*, 15(2), pp. 153-170.

Armitage, T. et al., 2017. Arctic Ocean surface geostrophic circulation 2003-2014. *Cryosphere*, 11(4), pp. 1767-1780.

Armitage, T. & Davidson, M., 2014. Using the Interferometric Capabilities of the ESA Cryosat-2 Mission to Improve the Accuracy of Sea Ice Freeboard Retrievals. *IEEE Trans. Geosci. Rem. Sens.*, 52(1), pp. 529-536.

Bacon, S., Aksenov, Y., Fawcett, S. & Madec, G., 2015. Arctic mass, freshwater and heat fluxes: methods and modelled seasonal variability. *Phil. Trans. Royal Soc. A*, Volume 373.

Blockley, E. & Peterson, K., 2018. Improving Met Office seasonal predictions of Arctic sea ice using assimilation of CryoSat-2 thickness. *Cryosphere*, 12(11), pp. 3419-3438.

Bouffard, J. et al., 2018. CryoSat instrument performance and ice product quality status. *Ad. Space Res.*, 62(6), pp. 1526-1548.

Breivik, L., Eastwood, S. & Lavergne, T., 2012. Use of C-band scatterometer for sea ice edge identification. *IEEE Trans. Geosci. Rem. Sens.*, 50(7), pp. 1669-2677.

Brodzik, M. et al., 2012. EASE-Grid 2.0: Incremental but significant improvements for Earth-gridded data sets. *ISPRS Int. J. Geo-Inf.*, 1(1), pp. 32-45.

Castro-Morales, K. et al., 2014. Sensitivity of simulated Arctic sea ice to realistic ice thickness distributions and snow parameterizations. *J. Geophys. Res. Oceans*, 119(1), pp. 559-571.

Chelton, D., Schlax, M. & Samelson, R., 2011. Global observations of nonlinear mesoscale eddies. *Progress in oceanography,* 91(2), pp. 167-216.

Di Bella, A. et al., 2020. Multi-peak Retracking of CryoSat-2 SARIn Waveforms Over Arctic Sea Ice. *IEEE Trans. Geosci. Rem. Sens.*.

Di Bella, A., Skourup, H., Bouffard, J. & Parrinello, T., 2018. Uncertainty reduction of Arctic sea ice freeboard from CryoSat-2 interferometric mode. *Adv. Space Res.*, 62(6), pp. 1251-1264.

Ducet, N., Le Traon, P. & Reverdin, G., 2000. Global high-resolution mapping of ocean circulation from TOPEX/Poseidon and ERS-1 and-2. *J. Geophys. Res. Oceans,* 105(C8), pp. 19477-19498.

Fichefet, T. & Morales Maqueda, M., 1997. Sensitivity of a global sea ice model to the treatment of ice thermodynamics and dynamics. *J. Geophys. Res. Oceans,* Volume 102, pp. 12609-12646.

Fritzner, S. et al., 2019. Impact of assimilating sea ice concentration, sea ice thickness and snow depth in a coupled ocean-sea ice modelling system. *Cryosphere,* 13(2), pp. 491-509.

Goosse, H. & Fichefet, T., 1999. Importance of ice-ocean interactions for the global ocean circulation: A model study. *J. Geophys. Res. Oceans`,* Volume 104, p. 23337–23355.

Guerreiro, K. et al., 2017. Comparison of CryoSat-2 and ENVISAT radar freeboard over Arctic sea ice: toward an improved Envisat freeboard retrieval. *Cryosphere,* 11(5), pp. 2059-2073.

Hutchings, J., Roberts, A., Geiger, C. & Richter-Menge, J., 2011. Spatial and temporal characterization of sea-ice deformation. *Ann. Glaciol.,* 52(57), pp. 360-368.

Jacobs, G., Barron, C. & Rhodes, R., 2001. Mesoscale characteristics. *J. Geophys. Res. Oceans,* 106(C9), pp. 19581-19595.

Kelly, S. et al., 2019. On the Origin of Water Masses in the Beaufort Gyre. *J. Geophys. Res. Oceans,* 124(7), pp. 4696-4709.

Kern, M. et al., 2020. The Copernicus Polar Ice and Snow Topography Altimeter (CRISTAL) high-priority candidate mission. *Cryosphere,* 14(7), pp. 2235-2251.

Kvas, A. et al., 2019. *The satellite-only gravity field model GOCO06s,* Potsdam: GFZ Data Services.

Kwok, R., 2018. Arctic sea ice thickness, volume, and multiyear ice coverage: losses and coupled variability (1958–2018). *Env. Res. Lett.,* 13(10), p. 105005.

Kwok, R. & Cunningham, G., 2015. Variability of Arctic sea ice thickness and volume from Cryosat-2. *Phil. Trans. R. Soc. A,* 373(20140157).

Kwok, R., Cunningham, G., Zwally, H. & Yi, D., 2007. Ice, Cloud, and land Elevation Satellite (ICESat) over Arctic sea ice: Retrieval of freeboard. *J. Geophys. Res.,* Volume 112, p. C12013.

Kwok, R. et al., 2020. Arctic snow depth and sea ice thickness from ICESat-2 and CryoSat-2 freeboards: A first examination. *J. Geophys. Res. Oceans,* 125(3).

Kwok, R. et al., 2019. Surface height and sea ice freeboard of the Arctic Ocean from ICESat-2: Characteristics and early results. *J. Geophys. Res. Oceans,* 124(10), pp. 6942-6959.

Landy, J. et al., 2017. Sea ice thickness in the Eastern Canadian Arctic: Hudson Bay Complex & Baffin Bay. *Rem. Sens. Env.,* Volume 200, pp. 281-294.

Landy, J. et al., 2017. Sea ice thickness in the Eastern Canadian Arctic: Hudson Bay Complex & Baffin Bay. *Rem. Sens. Env.,* Volume 200, pp. 281-294.

Landy, J., Petty, A., Tsamados, M. & Stroeve, J., 2020. Sea ice roughness overlooked as a key source of uncertainty in CryoSat-2 ice freeboard retrievals. *J. Geophys. Res. Oceans,* 125(5), p. e2019JC015820.

Landy, J., Tsamados, M. & Scharien, R., 2019. A Facet-Based Numerical Model for Simulating SAR Altimeter Echoes from Heterogeneous Sea Ice Surfaces. *IEEE Trans. Geosci. Rem. Sens.,* 57(7), pp. 4164-4180.

Lavergne, T. et al., 2019. Version 2 of the EUMETSAT OSI SAF and ESA CCI sea-ice concentration climate data records. *Cryosphere,* Volume 13, pp. 49-78.

Lawrence, I. et al., 2019. Extending the Arctic sea ice freeboard and sea level record with the Sentinel-3 radar altimeters. *Adv. Space Sci.,* Volume In Press.

Lawrence, I. et al., 2018. Estimating snow depth over Arctic sea ice from calibrated dual-frequency radar freeboards. *Cryosphere,* 12(11), pp. 3551-3564..

Laxon, S. et al., 2013. CryoSat-2 estimates of Arctic sea ice thickness and volume. *Geophys. Res. Lett.,* Volume 40, pp. 732-737.

Laxon, S., Peacock, N. & Smith, D., 2003. High interannual variability of sea ice thickness in the Arctic region. *Nature,* 425(6961), pp. 947-950.

Le Traon, P. et al., 2003. Can we merge GEOSAT follow-on with TOPEX/Poseidon and ERS-2 for an improved description of the ocean circulation?. *J. Atmos. Ocean. Tech.,* 20(6), pp. 889-895.

Le Traon, P., Nadal, F. & Ducet, N., 1998. An improved mapping method of multisatellite altimeter data. *J. Atmos. Ocean. Tech.,* 15(2), pp. 522-534.

Lee, S. et al., 2016. Arctic sea ice thickness estimation from CryoSat-2 satellite data using machine learning-based lead detection. *Rem. Sens.,* 8(9), p. 698.

Madec, G., Delecluse, P., Imbard, M. & Lévy, C., 1998. *OPA 8.1 Ocean General Circulation Model reference manual,* France: Institut Pierre-Simon Laplace (IPSL), Note du Pole de Modélisation.

Madec, G. & Imbard, M., 1996. A global ocean mesh to overcome the North Pole singularity. *Clim. Dyn.,* Volume 12, pp. 381-388.

Mallett, R. et al., 2020. Brief communication: Conventional assumptions involving the speed of radar waves in snow introduce systematic underestimates to sea ice thickness and seasonal growth rate estimates. *Cryosphere,* 14(1), pp. 251-260.

Manucharyan, G. & Spall, M., 2016. Wind-driven freshwater buildup and release in the Beaufort Gyre constrained by mesoscale eddies. *Geophys. Res. Lett.,* 43(1), pp. 273-282.

Markus, T. et al., 2017. The Ice, Cloud, and land Elevation Satellite-2 (ICESat-2): science requirements, concept, and implementation. *Rem. Sens. Env.,* Volume 190, pp. 260-273.

Massonnet, F., Fichefet, T. & Goosse, H., 2015. Prospects for improved seasonal Arctic sea ice predictions from multivariate data assimilation. *Ocean Mod.,* Volume 88, pp. 16-25.

Melia, N., Haines, K. & Hawkins, E., 2016. Sea ice decline and 21st century trans-Arctic shipping routes. *Geophys. Res. Lett.,* 43(18), pp. 9720-9728.

Meloni, M. et al., 2020. CryoSat Ice Baseline-D validation and evolutions. *Cryosphere,* 14(6), pp. 1889-1907.

Meneghello, G., Marshall, J., Cole, S. & Timmermans, M., 2017. Observational inferences of lateral eddy diffusivity in the halocline of the Beaufort Gyre. *Geophys. Res. Lett.,* 44(24), pp. 12331-12338.

Msadek, R., Vecchi, G., Winton, M. & Gudgel, R., 2014. Importance of initial conditions in seasonal predictions of Arctic sea ice extent. *Geophys. Res. Lett.,* 41(14), pp. 5208-5215.

Newman, T. et al., 2014. Assessment of radar-derived snow depth over Arctic sea ice. *J. Geophys. Res. Oceans,* 119(12), pp. 8578-8602.

Nurser, A. & Bacon, S., 2014. The rossby radius in the Arctic Ocean. *Ocean Sci.,* 10(6), pp. 967-975.

Paden, J. et al., 2017. *IceBridge Ku-Band Radar L1B Geolocated Radar Echo Strength Profiles, Version 2,* Boulder, Colorado, USA: NASA National Snow and Ice Data Center Distributed Active Archive Center.

Parkinson, C. & DiGirolamo, N., 2016. New visualizations highlight new information on the contrasting Arctic and Antarctic sea-ice trends since the late 1970s. *Rem. Sens. Env.,* Volume 183, pp. 198-204.

Parrinello, T. et al., 2018. CryoSat: ESA's ice mission–Eight years in space. *Adv. Space Sci.,* 62(6), pp. 1178-1190.

Passaro, M., Müller, F. & Dettmering, D., 2018. 2018. *Adv. Space Sci.,* Volume 62, pp. 1610-1625.

Paul, S. et al., 2018. Empirical parametrization of Envisat freeboard retrieval of Arctic and Antarctic sea ice based on CryoSat-2: progress in the ESA Climate Change Initiative. *Cryosphere,* 12(7), pp. 2437-2460.

Petty, A. et al., 2020. Winter Arctic Sea Ice Thickness From ICESat-2 Freeboards. *J. Geophys. Res. Oceans,* 125(5), p. e2019JC015764.

Poisson, J. et al., 2018. Development of an ENVISAT altimetry processor providing sea level continuity between open ocean and Arctic leads. *IEEE Trans. Geosci. Remote Sens.,* Volume 56, pp. 5299-5319.

Pujol, M. et al., 2016. DUACS DT2014: the new multi-mission altimeter data set reprocessed over 20 years. *Ocean Sci.,* 12(5), pp. 1067-1090.

Quartly, G. D. et al., 2019. Retrieving Sea Level and Freeboard in the Arctic: A Review of Current Radar Altimetry Methodologies and Future Perspectives. *Rem. Sens.,* 11(7), p. 881.

Rae, J. et al., 2014. A sensitivity study of the sea ice simulation in the global coupled climate model, HadGEM3. *Ocean Mod.,* Volume 74, pp. 60-76.

Ricker, R. et al., 2014. Sensitivity of CryoSat-2 Arctic sea-ice freeboard and thickness on radar-waveform interpretation. *Cryosphere,* Volume 8, pp. 1607-1622.

Rinne, E. & Similä, M., 2016. Utilisation of CryoSat-2 SAR altimeter in operational ice charting. *Cryosphere,* 10(1), pp. 121-131.

Rodriguez-Morales, F. et al., 2013. Advanced multifrequency radar instrumentation for polar research. *IEEE Trans. Geosci. Rem. Sens.,* 52(5), pp. 2824-2842.

Sallila, H., Farrell, S., McCurry, J. & Rinne, E., 2019. Assessment of contemporary satellite sea ice thickness products for Arctic sea ic. *Cryosphere,* 13(4), pp. 1187-1213.

Schröder, D. et al., 2019. New insight from CryoSat-2 sea ice thickness for sea ice modelling. *Cryosphere,* Volume 13, pp. 125-139.

Stroeve, J., Schroder, D., Tsamados, M. & Feltham, D., 2018. Warm winter, thin ice?. *Cryosphere,* 12(5), pp. 1791-1809.

Stroeve, J. et al., 2021. A mulit-sensor and modelling approach for mapping light under sea ice. *Front. Mar. Sci.*.

Tilling, R., Ridout, A. & Shepherd, A., 2018. Estimating Arctic sea ice thickness and volume using CryoSat-2 radar altimeter data. *Adv. Space Res.,* 62(6), pp. 1203-1225.

Tschudi, M., Stroeve, J. & Stewart, J., 2016. Relating the age of Arctic sea ice to its thickness, as measured during NASA's ICESat and IceBridge campaigns. *Rem. Sens.,* 8(6), p. 457.

Tsubouchi, T. et al., 2018. The Arctic Ocean Seasonal Cycles of Heat and Freshwater Fluxes: Observation-Based Inverse Estimates. *J. Phys. Oceanogr.,* Volume 48, pp. 2029-2055.

Wernecke, A. & Kaleschke, L., 2015. Lead detection in Arctic sea ice from CryoSat-2: quality assessment, lead area fraction and width distribution. *Cryosphere,* 9(5), pp. 1955-1968.

Willatt, R. et al., 2011. Ku-band radar penetration into snow cover on Arctic sea ice using airborne data. *Ann. Glaciol.,* 52(57), pp. 197-205.

Wingham, D. et al., 2006. CryoSat: A mission to determine the fluctuations in Earth's land and marine ice fields. *Adv. Space Res.,* 37(4), pp. 841-871.

Xia, W. & Xie, H., 2018. Assessing three waveform retrackers on sea ice freeboard retrieval from Cryosat-2 using Operation IceBridge Airborne altimetry datasets. *Rem. Sens. Env.,* Volume 204, pp. 456-471.

Figure 1. Schematic diagram illustrating the conventional and proposed new methods for interpolating the sea surface height at sea ice locations. In the conventional approach only the four leads along the central track (yellow footprints) are used to interpolate SSH at the sea ice floe location (green footprint). In the proposed approach, all 14 leads (yellow plus blue footprints) acquired within ±2 days at neighboring tracks inside a prescribed sea surface height covariance limit (green circle) around the ice floe are used to compute the SSH. Background is a SAR image from Sentinel-1.

Figure 2. Mean October-April surface geostrophic currents [km/day] for the sea ice-covered region of the Arctic Ocean

Figure 3. (a) Echogram from the OIB Ku-band radar over MYI in the Lincoln Sea on March 26th 2014, compensated for aircraft altitude changes and relative to the WGS-84 ellipsoid, including the retracked elevation of the snow-sea ice interface, samples classified as leads, and an estimate for the sea surface height. (b) Radar freeboards derived from the difference between snow-ice interface elevation and sea level, averaged onto the footprint locations of a coincident CryoSat-2 overpass.

Figure 4. Mean e-folding decorrelation length scales of the Arctic Ocean sea level anomaly (SLA) for (a) the zonal direction, (b) meridional direction, and (c) time, calculated from the full 2010-2019 archive of CryoSat-2 sea surface height estimates at leads. (d) First mode of the annual-mean baroclinic Rossby radius derived from the Polar Science Center Hydrographic Climatology and reproduced from (Nurser & Bacon, 2014).

Figure 5. Mean (a) covariance amplitude and (b) covariance at zero lag for the time-dependent sea surface height signal obtained from CryoSat-2 2010-2019. These maps illustrate the standard deviation of the SLA outside the correlation timescale (Fig. 4c) and, in contrast, the measurement noise when there is no time lag, respectively.

Figure 6. Theoretical covariance function of the sea surface height (SSH) signal imposed within the objective mapping method (a) as a function of time and distance, and (b) distance only for t = 0. Here $L_x = L_y$ = 200 km, T = 10 days, $P_x = P_y = 0$.

Figure 7. a) Profile of retracked surface elevation estimates from a SAR-mode CryoSat-2 track on 3rd March 2013 (03:46:51 UTC), with respect to the locally computed mean sea surface (i.e. SLA), with an estimate for the local instantaneous sea level and uncertainty derived from a conventional approach. (b) Covariances between the CryoSat-2 observation location and nearby leads on- and off-track, with the

final objective estimate for the sea level and uncertainty. (c) Final objective sea level and uncertainty over the CryoSat-2 elevation estimates, as in (a), and inset map of the track location (annotations referred to in text). (d) Sea ice radar freeboards derived with the conventional and new objective methods for deriving the SSH, and the long wavelength correlated differences between them.

Figure 8. Pan-Arctic analysis of the conventional and new methods for deriving ice freeboards in March 2013. (a) 25-km gridded distribution of CryoSat-2 radar freeboards from the objective mapping SSH method minus the conventional approach, including the limit of the multi-year sea ice area in black. (b) Radar freeboard differences between the two methods, from the raw along-track CryoSat-2 sea ice observations. (c) Ratio of the SSH uncertainty estimate from the objective mapping method to the conventional along-track uncertainty estimate, also from the along-track observations.

Figure 9. Analysis of paired (a) sea surface height and (b) radar freeboard differences at orbital crossover locations of CryoSat-2 in March 2013. All crossover locations within one day and a maximum distance of 5 km are illustrated in (c).

Figure 10. a) Profile of retracked surface elevation estimates from a SARIn-mode CryoSat-2 track on 26th March 2012 (15:45:42 UTC), with respect to the mean sea surface (i.e. SLA); covariances to local lead observations on- and off-track; and the objective sea level and uncertainty estimates. (b) Conventional and objective SSH estimates with their uncertainty (precision) envelopes. (c) Coincident radar freeboards from the CReSIS airborne Ku-band radar and CryoSat-2 processed with the two methods, including a map of the coinciding section (in red) inset. (d) and (e) Probability density functions (PDFs) of the airborne and satellite radar freeboard observations, processed with conventional and objective methods for deriving the SSH.

Figure 11. a) Profile of retracked surface elevation estimates from a SAR-mode CryoSat-2 track on 26th March 2014 (09:06:49 UTC), with respect to the mean sea surface (i.e. SLA); covariances to local lead observations on- and off-track; and the objective sea level and uncertainty estimates. (b) Conventional and objective SSH estimates with their uncertainty (precision) envelopes. (c) Coincident radar freeboards from the CReSIS airborne Ku-band radar and CryoSat-2 processed with the two methods, including a map of the coinciding section (in red) inset. (d) and (e) Probability density functions (PDFs) of the airborne and satellite radar freeboard observations, processed with conventional and objective methods for deriving the SSH.

Figure 1.

t + 1

5 km

t - 2

t = 0

t + 2

Figure 2.

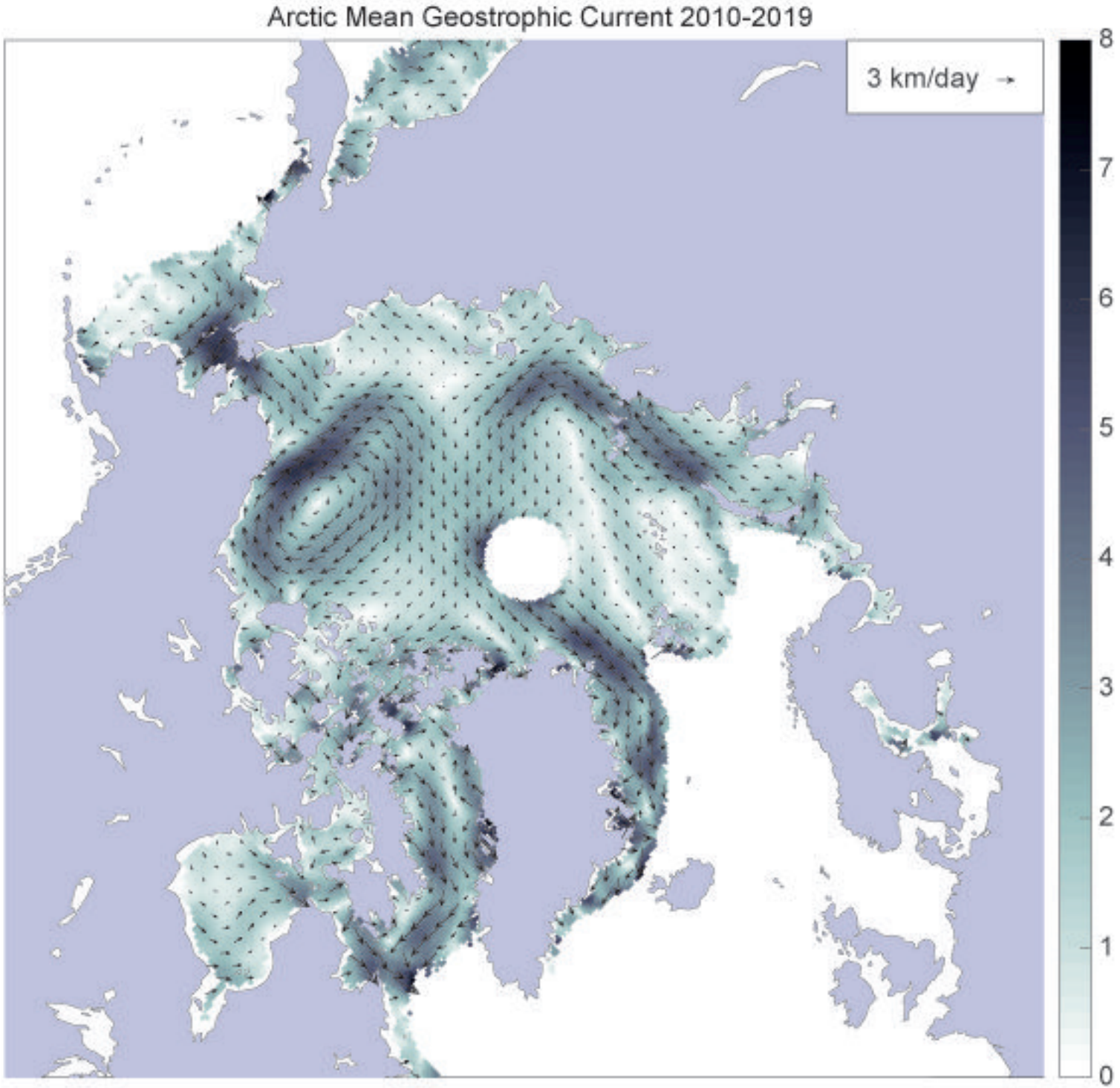
Arctic Mean Geostrophic Current 2010-2019
3 km/day
8
7
6
5
4
3
2
1
0

Figure 3.

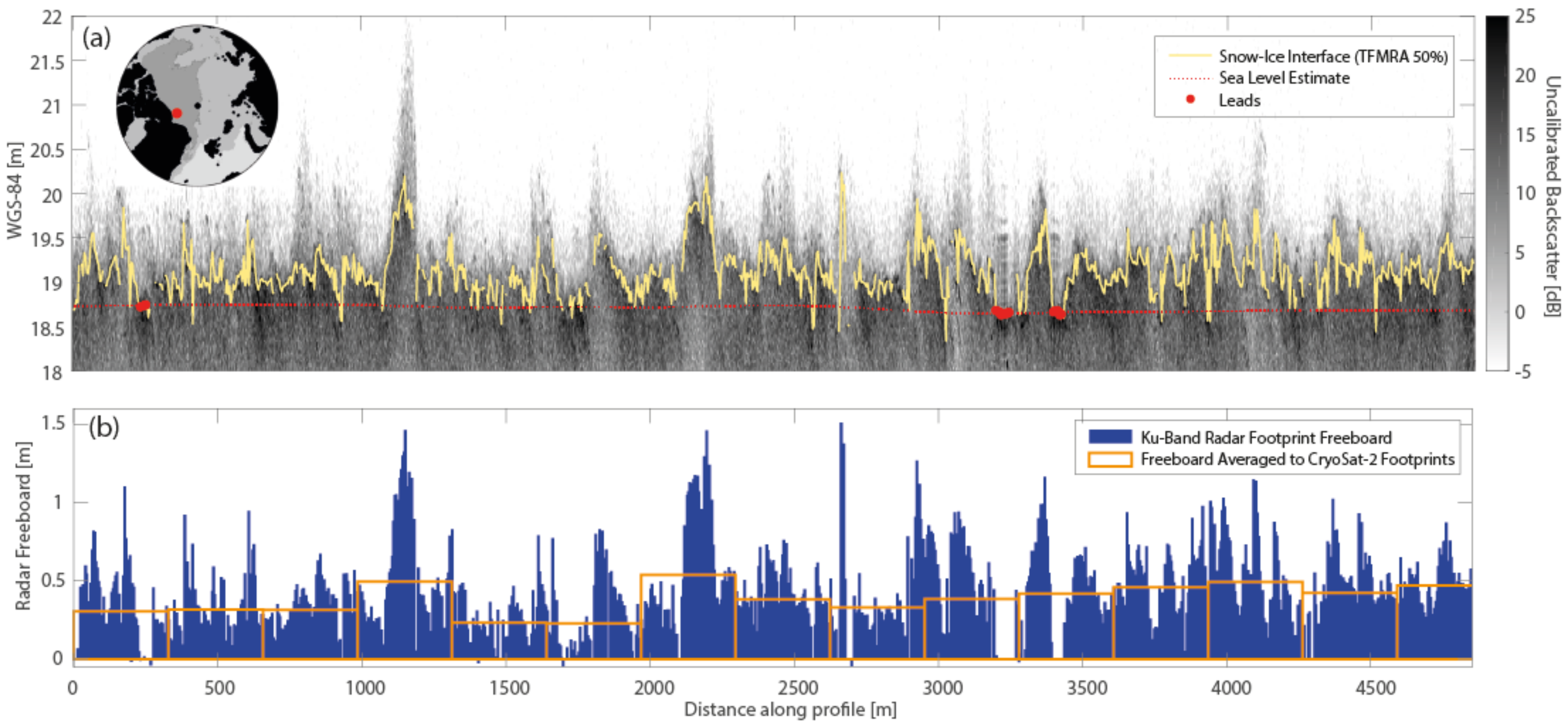
(a)
Snow-Ice Interface (TFMRA 50%)
Sea Level Estimate
Leads
WGS-84 [m]
Uncalibrated Backscatter [dB]
(b)
Ku-Band Radar Footprint Freeboard
Freeboard Averaged to CryoSat-2 Footprints
Radar Freeboard [m]
Distance along profile [m]

Figure 4.

Zonal Decorrelation Length Scale of the Sea Level Anomaly

(a)

220 km
200
180
160
140
120
100
80
60
40

Meridional Decorrelation Length Scale of the Sea Level Anomaly

(b)

220 km
200
180
160
140
120
100
80
60
40

Temporal Decorrelation Length Scale of the Sea Level Anomaly

(c)

6 days
5
4
3
2
1

Annual-Mean Rossby Radius Mode 1

(d)

14 km
12
10
8
6
4
2

Figure 5.

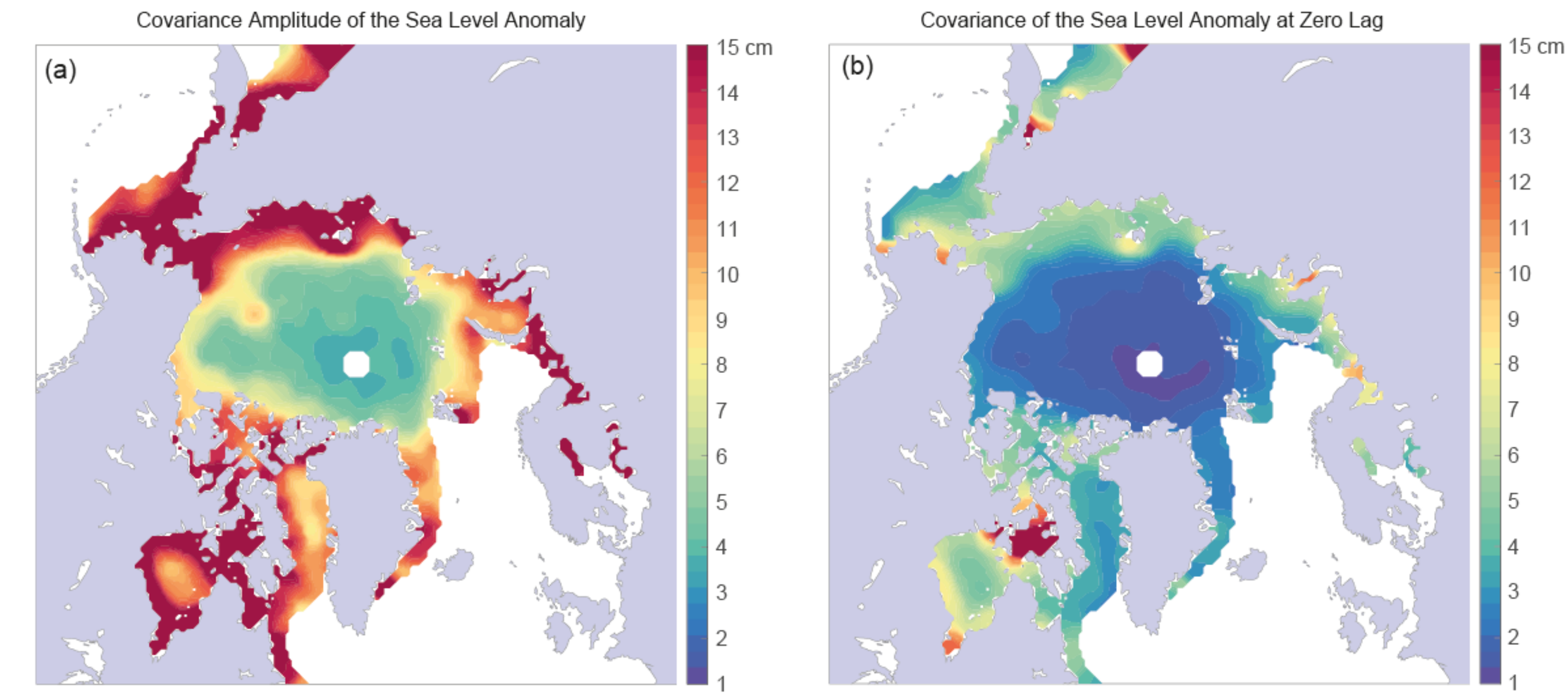
Covariance Amplitude of the Sea Level Anomaly
(a)
15 cm
14
13
12
11
10
9
8
7
6
5
4
3
2
1
Covariance of the Sea Level Anomaly at Zero Lag
(b)
15 cm
14
13
12
11
10
9
8
7
6
5
4
3
2
1

Figure 6.

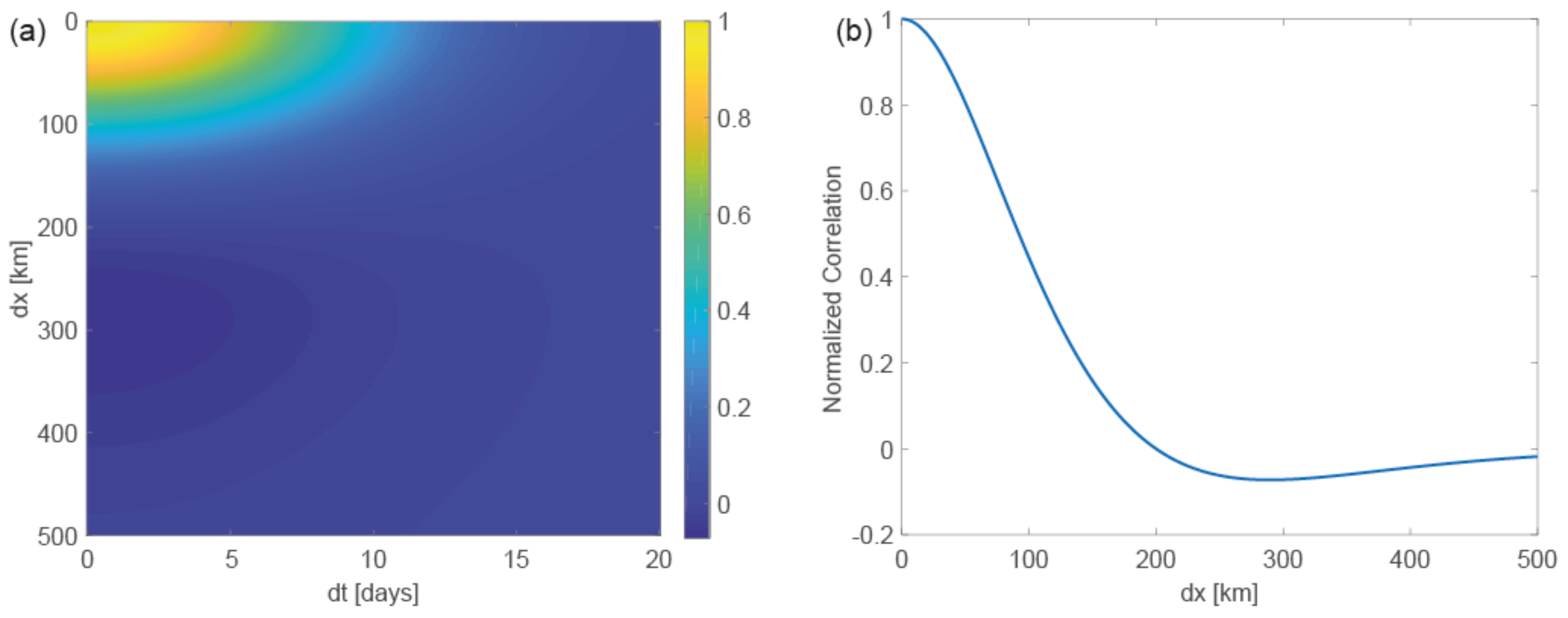
(a)
0
100
200
300
400
500
dx [km]
0
5
10
15
20
dt [days]
1
0.8
0.6
0.4
0.2
0
(b)
1
0.8
0.6
0.4
0.2
0
-0.2
Normalized Correlation
0
100
200
300
400
500
dx [km]

Figure 7.

(a)

SLA [m]

CryoSat-2 Retracked Heights
10-km Moving Average
Conventional Sea Level Estimate
Sea Level Uncertainty
Lead Observations on Track

(b)

SLA [m]

Covariance with Proximal Leads
Objective Sea Level Estimate
Sea Level Uncertainty
Lead Observations on Track

(c)

SLA [m]

(i)
(ii)
(iii)

(d)

Radar Freeboard [m]

Radar Freeboard with Conventional Method
Radar Freeboard with New Method
Radar Freeboard Difference

Distance Along Orbit [km]

Figure 8.

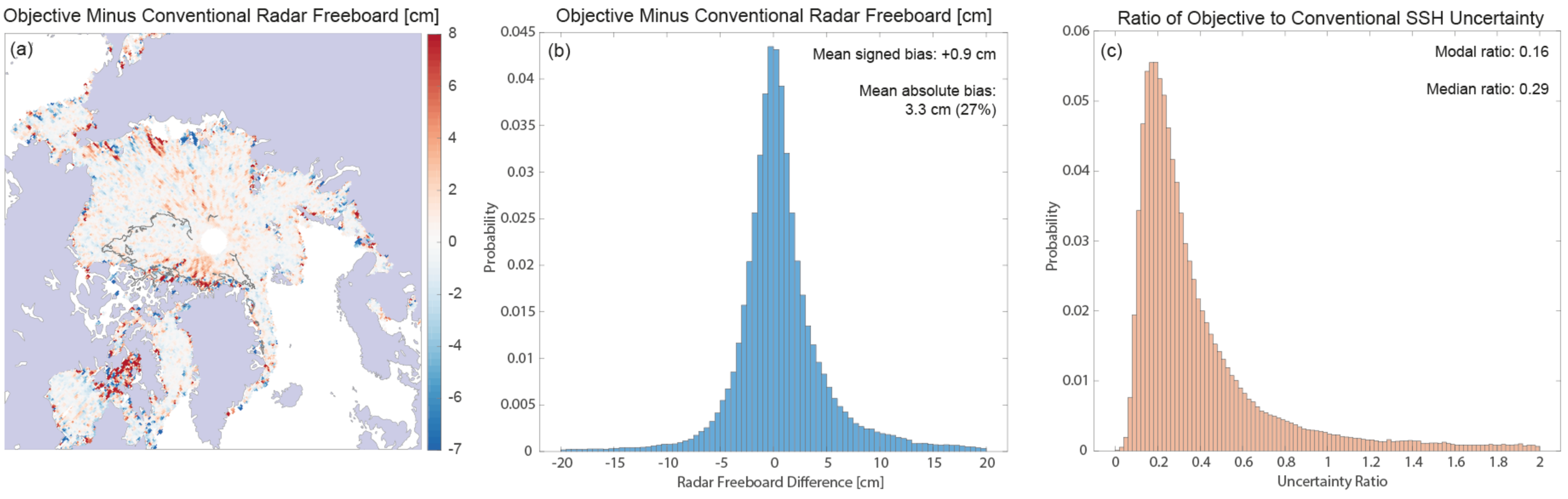
Objective Minus Conventional Radar Freeboard [cm]
(a)
8
6
4
2
0
-2
-4
-6
-7
Objective Minus Conventional Radar Freeboard [cm]
(b)
Mean signed bias: +0.9 cm
Mean absolute bias:
3.3 cm (27%)
Probability
0.045
0.04
0.035
0.03
0.025
0.02
0.015
0.01
0.005
0
-20
-15
-10
-5
0
5
10
15
20
Radar Freeboard Difference [cm]
Ratio of Objective to Conventional SSH Uncertainty
(c)
Modal ratio: 0.16
Median ratio: 0.29
Probability
0.06
0.05
0.04
0.03
0.02
0.01
0
0
0.2
0.4
0.6
0.8
1
1.2
1.4
1.6
1.8
2
Uncertainty Ratio

Figure 9.

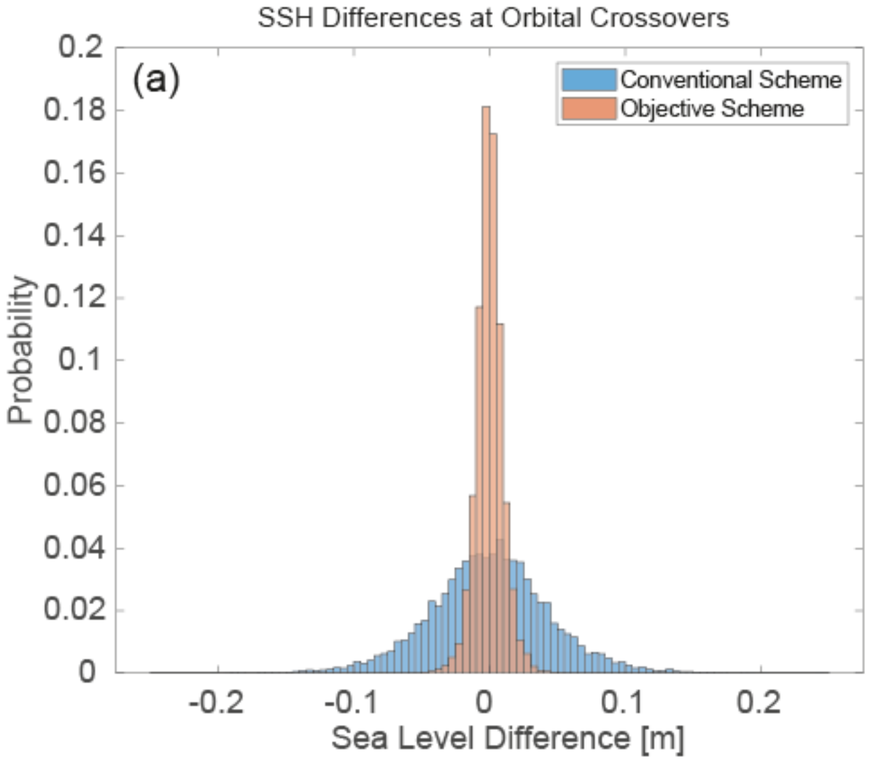
SSH Differences at Orbital Crossovers
(a)
Conventional Scheme
Objective Scheme
Probability
0.2
0.18
0.16
0.14
0.12
0.1
0.08
0.06
0.04
0.02
0
-0.2
-0.1
0
0.1
0.2
Sea Level Difference [m]

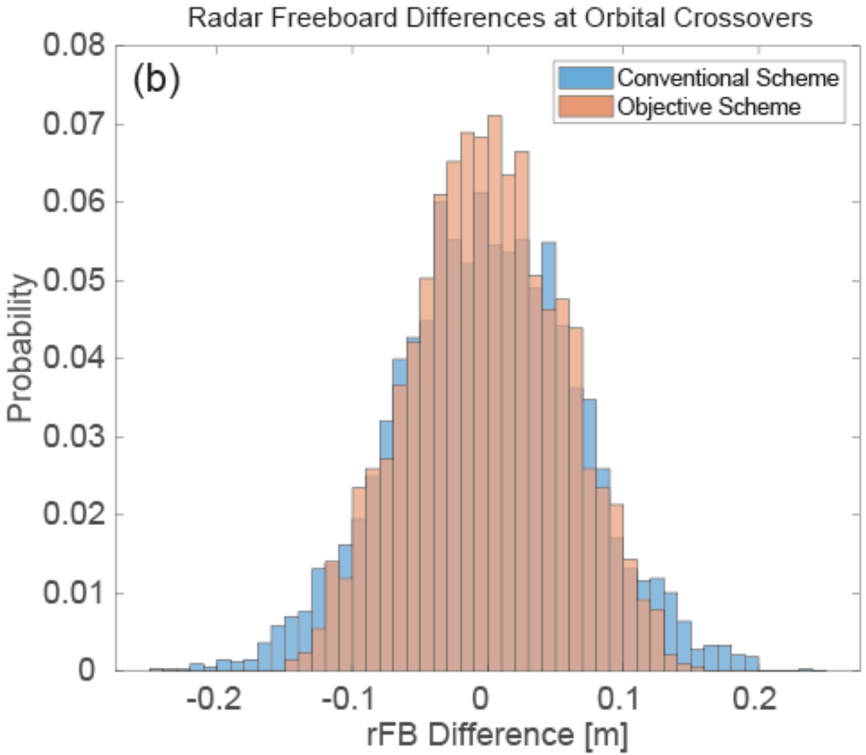
Radar Freeboard Differences at Orbital Crossovers
(b)
Conventional Scheme
Objective Scheme
Probability
0.08
0.07
0.06
0.05
0.04
0.03
0.02
0.01
0
-0.2
-0.1
0
0.1
0.2
rFB Difference [m]

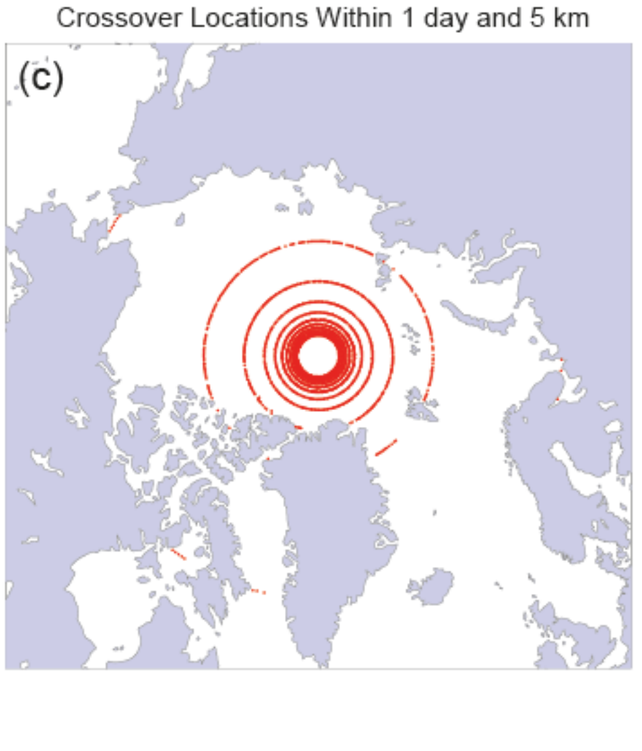
Crossover Locations Within 1 day and 5 km
(c)

Figure 10.

(a)
5-km Ice Floe Moving Average
Covariance with Proximal Leads
Objective Sea Level Estimate
Sea Level Uncertainty
SLA [m]
(b)
CryoSat-2 Retracked Heights
Conventional Sea Level Estimate
Sea Level Uncertainty
SLA [m]
(c)
OIB Radar Freeboard
CS2 Conventional
CS2 Objective Mapping
Radar Freeboard [m]
Distance Along Profile [km]
(d) Conventional SSH Method
OIB rFB
CS2 rFB
Probability
Radar Freeboard [m]
(e) Objective SSH Method
OIB rFB
CS2 rFB
Radar Freeboard [m]

Figure 11.

(a)

SLA [m]

5-km Ice Floe Moving Average
Covariance with Proximal Leads
Objective Sea Level Estimate
Sea Level Uncertainty

(b)

SLA [m]

CryoSat-2 Retracked Heights
Conventional Sea Level Estimate
Sea Level Uncertainty

(c)

Radar Freeboard [m]

OIB Radar Freeboard
CS2 Conventional
CS2 Objective Mapping

Distance Along Profile [km]

(d) Conventional SSH Method

Probability

OIB rFB
CS2 rFB

Radar Freeboard [m]

(e) Objective SSH Method

OIB rFB
CS2 rFB

Radar Freeboard [m]